Comparison between Observed and Simulated AgI Seeding Impacts in a Well-Observed Case from the SNOWIE Field Program

Lulin Xue, ^a Courtney Weeks, ^a Sisi Chen, ^a Sarah A. Tessendorf, ^a Roy M. Rasmussen, ^a Kyoko Ikeda, ^a Branko Kosovic, ^a Dalton Behringer, ^b Jeffery R. French, ^b Katja Friedrich, ^c Troy J. Zaremba, ^d Robert M. Rauber, ^d Christian P. Lackner, ^b Bart Geerts, ^b Derek Blestrud, ^e Melvin Kunkel, ^e Nick Dawson, ^e and Shaun Parkinson ^e

a Research Applications Laboratory, National Center for Atmospheric Research, Boulder, Colorado
 b Department of Atmospheric Science, University of Wyoming, Laramie, Wyoming
 c Department of Atmospheric and Oceanic Sciences, University of Colorado Boulder, Boulder, Colorado
 d Department of Atmospheric Sciences, University of Illinois at Urbana–Champaign, Urbana, Illinois
 c Idaho Power Company, Boise, Idaho

(Manuscript received 3 June 2021, in final form 17 December 2021)

ABSTRACT: A dry-air intrusion induced by the tropopause folding split the deep cloud into two layers resulting in a shallow orographic cloud with a supercooled liquid cloud top at around -15° C and an ice cloud above it on 19 January 2017 during the Seeded and Natural Orographic Wintertime Clouds: The Idaho Experiment (SNOWIE). The airborne AgI seeding of this case was simulated by the WRF Weather Modification (WRF-WxMod) Model with different configurations. Simulations at different grid spacing, driven by different reanalysis data, using different model physics were conducted to explore the ability of WRF-WxMod to capture the properties of natural and seeded clouds. The detailed model—observation comparisons show that the simulation driven by ERA5 data, using Thompson–Eidhammer microphysics with 30% of the CCN climatology, best captured the observed cloud structure and supercooled liquid water properties. The ability of the model to correctly capture the wind field was critical for successful simulation of the seeding plume locations. The seeding plume features and ice number concentrations within them from the large-eddy simulations (LES) are in better agreement with observations than non-LES runs mostly due to weaker AgI dispersion associated with the finer grid spacing. Seeding effects on precipitation amount and impacted areas from LES seeding simulations agreed well with radar-derived values. This study shows that WRF-WxMod is able to simulate and quantify observed features of natural and seeded clouds given that critical observations are available to validate the model. Observation-constrained seeding ensemble simulations are proposed to quantify the AgI seeding impacts on wintertime orographic clouds.

SIGNIFICANCE STATEMENT: Recent observational work has demonstrated that the impact of airborne glaciogenic seeding of orographic supercooled liquid clouds is detectable and can be quantified in terms of the extra ground precipitation. This study aims, for the first time, to simulate this seeding impact for one well-observed case. The stakes are high: if the model performs well in this case, then seasonal simulations can be conducted with appropriate configurations after validations against observations, to determine the impact of a seeding program on the seasonal mountain snowpack and runoff, with more fidelity than ever. High–resolution weather simulations inherently carry uncertainty. Within the envelope of this uncertainty, the model compares very well to the field observations.

KEYWORDS: Precipitation; Cloud microphysics; Orographic effects; Cloud seeding; Weather modification

1. Introduction

Wintertime orographic cloud seeding with silver iodide (AgI) particles has been utilized to address water resource and management problems in arid and semiarid regions around the world for decades, as a way to enhance precipitation (Rauber et al. 2019). Quantification of seeding effects on precipitation is a critical question for both research and operational cloud seeding programs (Rauber et al. 2019; Flossmann et al. 2019). Traditional statistical evaluation approaches are hampered by the large natural variability of precipitation, insufficient randomized experiments, and the high cost of conducting experiments that last years with enough cases to obtain statistically significant results

Corresponding author: Lulin Xue, xuel@ucar.edu

(Rauber et al. 2019). Although physical evidence of seeding impacts on clouds and precipitation have been collected in several field experiments, seeding impact on surface precipitation has only recently been quantified (Friedrich et al. 2020 2021). Numerical models that simulate both natural and seeding processes have proven to be useful and valuable in quantifying seeding effects (Xue et al. 2013a,b, 2014, 2016, 2017; Chu et al. 2014, 2017a,b; Rasmussen et al. 2018), but observations of seeding impacts on clouds and precipitation are needed to validate simulated seeding effects and further improve confidence in model results.

Two recent field campaigns focusing on wintertime orographic cloud seeding took advantage of advances in theory, instruments and modeling, and provided critical data and methods to advance our knowledge of glaciogenic seeding mechanisms and their impacts on wintertime orographic clouds and precipitation. The AgI Seeding Cloud Impact Investigation (ASCII) field program (Geerts et al. 2013; Pokharel and Geerts 2016) took place in southern Wyoming in early 2012 and early 2013 and had a goal to identify physical evidence of the impacts on orographic clouds of groundbased AgI seeding. ASCII piggybacked on the Wyoming Weather Modification Pilot Program (WWMPP), a statistical confirmatory cloud seeding research program (Breed et al. 2014; Rasmussen et al. 2018). ASCII deployed a ground station with a Doppler-on-Wheels (DOW) radar, located downwind of the AgI generators and a scanning radar to investigate the seeding impact. A unique aspect of this field campaign was the deployment of the University of Wyoming King Air (UWKA) equipped with a W-band Cloud Radar (WCR), Wyoming Cloud lidar (WCL) and a full suite of in situ microphysics instruments. Due to the safety limitations of flying near mountains and limits of vertical ground-based AgI dispersion, only the remote sensing data from the research aircraft could be used to analyze the seeding impact. The composite analysis of data during unseeded and seeded periods showed a positive impact of cloud seeding in terms of low-level radar reflectivity and snow particle concentration (Jing and Geerts 2015; Jing et al. 2015, 2017; Pokharel et al. 2014a,b, 2015, 2017), but the seeded versus unseeded compositing technique (mandated by the fact that no wellidentified plumes of enhanced reflectivity were present downwind of the AgI generators) inherently implied a relatively low confidence. Because of the lack of clear radar signatures, radar-based quantification of seeding-induced precipitation was not possible in ASCII. Detailed ASCII case simulations using the Weather Research and Forecasting (WRF) Model large-eddy simulation (LES) and an AgI cloud seeding parameterization (Xue et al. 2013a,b) showed that AgI particles released from ground-based generators are confined within the boundary layer height, determined by both the terrain-induced turbulence and the cloud buoyancy. Positive impacts were found for shallow stratified orographic clouds and clouds with embedded convection (Chu et al. 2014; Xue et al. 2016; Chu et al. 2017a,b). However, the magnitude and representativeness of the simulated seeding effect could not be validated.

The second field campaign, the Seeded and Natural Orographic Wintertime Clouds: The Idaho Experiment (SNOWIE), took place in central Idaho in the early 2017 (Tessendorf et al. 2019). Based on the lessons learned from the ASCII project, SNOWIE focused on detecting evidence of physical impacts when seeding occurred within the cloud layer (airborne AgI seeding), with a goal of using these data to verify models designed to simulate cloud seeding (Xue et al. 2013a,b). SNOWIE deployed the UWKA with radar, lidar and in situ microphysics probes, plus two ground-based DOW radars. Multiple microwave radiometers and fine-resolution snow gauges were also deployed in the experimental target area. More details on the field program can be found in Tessendorf et al. (2019). Direct evidence of microphysical impacts and precipitation effects by AgI (hereinafter referred to as seeding signatures/signals) were clearly observed in three intensive observed periods (IOPs) (French

et al. 2018; Tessendorf et al. 2019; Friedrich et al. 2020, 2021). These distinct seeding signatures allow us to perform a detailed comparison of observations with model simulations of seeding impact. This paper provides an in-depth model-observation analysis for the 19 January 2017 case, IOP5 of SNOWIE, during which an unambiguous seeding signature was observed (French et al. 2018).

This work demonstrates how detailed observations can be used to constrain numerical simulations, not just in terms of environmental and natural cloud conditions, but also, for the first time, in terms of AgI seeding effects on clouds and precipitation. Once the modeling framework and approach is proven effective, it can be used to determine the impacts of operational cloud seeding on surface precipitation, snowpack, and seasonal streamflow, for an entire winter season with unprecedented confidence as long as each seeding case simulation is adequately validated. The case and the data used in this study are described in the next section. The design and configurations of the numerical simulations are provided in section 3. Comparisons between the model-simulated natural/ seeded clouds/precipitation and observations are provided in section 4, followed by a discussion and conclusions in sections 5 and 6, respectively.

2. Case and data descriptions

a. SNOWIE IOP5

IOP5 on 19 January 2017 was the first SNOWIE case in which a clear seeding signature was observed by airborne, ground-based radars, and other instruments. The UWKA probed the early natural clouds from 1527 to 1640 UTC and continued to sample clouds that were seeded until 1832 UTC (red tracks in Fig. 1b). The airborne seeding operation took place from 1623 to approximately 1740 UTC (blue tracks in Fig. 1b) using the Weather Modification International (WMI) seeding aircraft, which flew normal to the UKWA track (Tessendorf et al. 2019). The DOW radar at Snowbank Mountain ("SB" in Fig. 1b) performed mostly volume scans while the DOW at Packer John Mountain ("PJ" in Fig. 1b) collected data from both volume and vertical cross-section scans. Details of the UWKA and WMI aircraft flights and DOW operations during IOP5 can be found in French et al. (2018) and Friedrich et al. (2021). In the following, we provide a brief description of the aircraft operations and a synoptic analysis to frame the conditions during the flights.

IOP5 began at 1200 UTC and continued through 1900 UTC, with 10 UWKA research flight legs executed between 1540 and 1821 UTC. The first three legs were completed before seeding started and were flown at 4.2 km MSL (540 hPa), while the remainder of the legs were flown at 3.9 and 3.6 km (570 and 590 hPa), 300–600 m below the altitude of the seeding aircraft. The seeding aircraft began operations at 3.9 km on its first leg, and then ascended to 4.2 km for the remainder of its flight. Winds across the region of operation were southwesterly between the surface and 4.2 km, increasing from 10 m s⁻¹ at the surface to 30 m s⁻¹ at the flight level. Above the flight level, winds changed to westerly, increasing to 60 m s⁻¹ at the

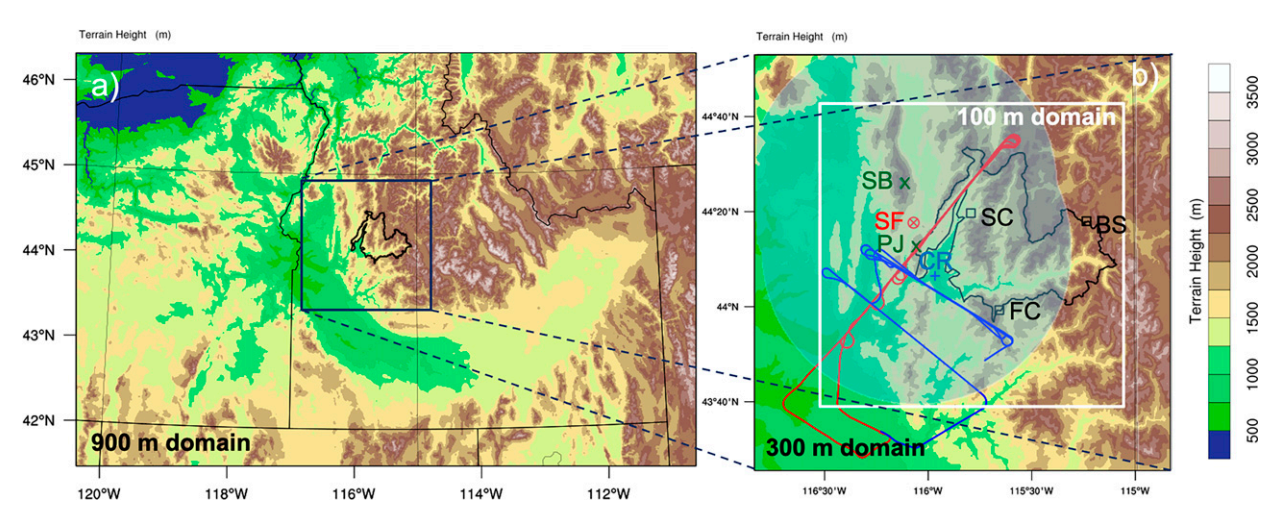


FIG. 1. Topography maps of the (a) 900-m domain and (b) 300- and 100-m domains. The Payette watershed (seeding target area) is outlined in black in both panels. The black-outlined box in (a) indicates the LES domain with 300-m grid spacing. The white box in (b) represents the LES domain with 100-m grid spacing. Red lines in (b) represent the UWKA flight tracks. The WMI seeding aircraft tracks are indicated in blue lines in (b). The DOWs at Snowbank (SB) and Packer John (PJ) are marked by green Xs in (b). The DOW detection range is shown by overlapping 50-km-radius circles in semitransparent blue. The red X enclosed by the red circle is the radiometer at Smith Ferry (SF). The blue plus sign shows the sounding location at Crouch (CR). Small open black squares indicate three high-resolution gauge sites at Silver Creek (SC), Five Corners (FC), and Banner Summit (BS).

tropopause (lowering from 9 to 8 km during the IOP). The UKWA flight track was oriented from southwest to northeast, parallel to the wind at flight level.

A season-long WRF simulations set from 1 October 2016 to 30 April 2017 was conducted to provide hourly meteorological information for SNOWIE analysis. The simulations were driven by the ERA5 reanalysis (Hersbach et al. 2020) over two nested domains with 2.7-km and 900-m grid spacing, respectively. Figure 2 shows the larger-scale meteorological conditions from the 2.7-km domain at four levels at 1600 UTC near the beginning of the operational period. We also examine vertical transects in Fig. 3. An upper-level trough is present near the U.S. West Coast, upstream of the area of interest in central Idaho (Fig. 2a). Ahead of the trough, a 45 m s⁻¹ south-north-oriented jet is present near the tropopause at 300 hPa; the axis of the jet is close to the region of the flight (Fig. 2a). A weak tropopause fold extends downward to ~6 km MSL (Fig. 3b), producing an upper-level front on its eastern flank (Fig. 2b). The circulation around this fold results in high-humidity, high- θ_e (equivalent potential temperature) air upward east of front (Fig. 3a), advected by the jet core from the south, producing a deep cloud layer with tops near the elevated tropopause (Figs. 3a,c). The effect of the intrusion of drier air associated with the passage of the upper-level frontal zone is to create decoupled cloud layers over the Payette Mountain region, one above 6 km, and the other below 4 km, during the airborne seeding period. At the time of the first and second UKWA flight legs (Fig. 3c), the deep cloud layer is present over the northeastern half of the study area, while the dry intrusion and split cloud layer is prominent over the southwestern half (Fig. 3c). During the flight, the deep cloud layer moves east and out of the study domain, together with the progression of the tropopause fold. It was

within the lower cloud layer, with cloud tops near 4.5 km (-15°C) , that all seeding operations took place.

b. Observational data

For this model-observation comparison study, the sounding data from Crouch ("CR" in Fig. 1b) was used to validate the model-simulated environmental conditions. The radiometer liguid water path (LWP) observations at Smith Ferry (red circle with enclosed "X" in Fig. 1b) were used to validate the supercooled LWP in the seeding region simulated by the WRF Weather Modification (WRF-WxMod) system (Xue et al. 2013a,b, see description below). The UWKA in situ microphysics and atmospheric state measurements were used to validate the modeled cloud-microphysical properties and environmental conditions. The UWKA WCR/WCL remote sensing data were used to compare modeled cloud structure and phase in natural and seeded clouds. The reflectivity fields from two DOW radars were used to validate simulated seeding plume properties. The precipitation data from three quality-controlled high-resolution snow gauge sites (black squares in Fig. 1b) and the derived snowfall from DOW reflectivity were used to validate model precipitation amount and distributions from natural and seeded clouds.

3. Model description and experimental design

a. WRF-WxMod

WRF-WxMod (pronounced as "WRF weather mod") is a modeling system based on the WRF Model that includes several cloud-seeding parameterizations to explicitly simulate the interactions between AgI and cloud hydrometeors (Xue et al. 2013a; Rauber et al. 2019; Geresdi et al. 2017, 2020) and a family of wintertime AgI seeding case-calling algorithms to provide seeding operation decision support. The cloud-seeding

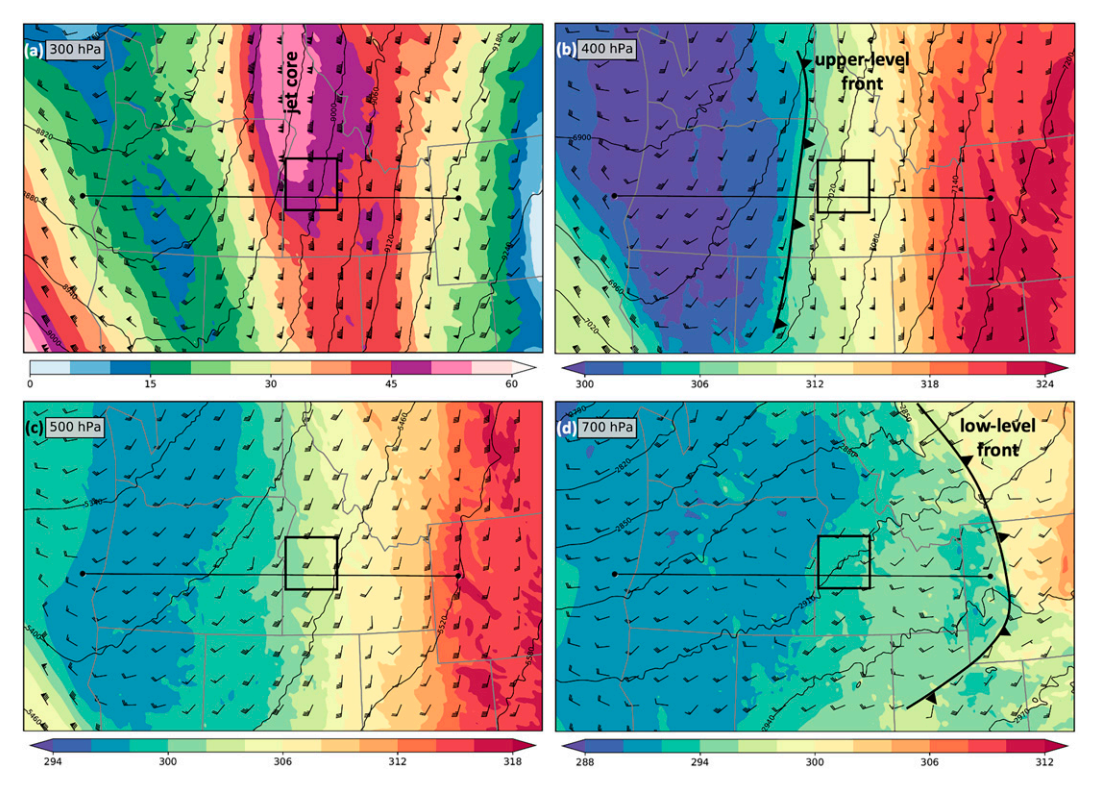


FIG. 2. Geopotential height (solid lines; m), and winds (full barb = 5 m s^{-1}) at 1600 UTC 19 Jan 2017 at (a) 300, (b) 400, (c) 500, and (d) 700 hPa. The color fill is wind speed (m s⁻¹) in (a) and potential temperature (K) in (b)–(d). State borders are in gray, and the black-outlined box is the 100-m model domain. The black horizontal line marks the location of the transect in Fig. 3, below.

parameterization described in Xue et al. (2013a) uses the bulk Thompson microphysical scheme (Thompson et al. 2008) with modification to include AgI cloud seeding. A schematic describing the interactions between AgI particles and cloud hydrometeors in the version coupled to the Thompson-Eidhammer scheme (Thompson and Eidhammer 2014) is shown in Fig. 4 [adapted from Fig. 7 in Rauber et al. (2019)]. As compared with the version documented in Xue et al. (2013a), the current version implements the following additional processes for interactions between AgI particles and hydrometeors: the self-coagulation of dry AgI particles, impact scavenging of AgI particles by precipitation particles (rain, snow and graupel), and dry deposition of AgI particles through fallout and canopy interception. This updated cloud seeding parameterization was used to simulate the SNOWIE IOP5 in this study. More details on WRF-WxMod can be found online (https://ral.ucar.edu/ solutions/products/wrf-wxmod).

b. Numerical experimental design

Our previous work has demonstrated that LES at 300- and 100-m grid spacing reliably captures the cloud development and dispersion of AgI particles from ground generators (e.g., Xue et al. 2014, 2016; Chu et al. 2017a,b). The successful LES of dispersion and cloud/precipitation formation over complex terrain requires high-resolution topography data. In this

study, USGS 1 arc-s terrain data (~30-m resolution) were used for the LES with 300- and 100-m grid spacing (Fig. 1b). When running the atmospheric model over complex terrain, numerical instabilities arise in the horizontal pressure gradient term close to the ground over steep slopes (Mahrer 1984). When the terrain slope is above 45°, the numerics typically break down (Mahrer 1984). Even for slopes between ~30° and 45°, models may crash if the time step is not small enough. Therefore, we applied a strategy to reduce localized steep slopes through local filtering. The filtered topography still keeps most of the details of the topography but reduces the extreme slopes. With this treatment, we were able to achieve stable simulations using the time step of 1/3 and 1/9 s for the 300- and 100-m domains, respectively.

To provide good-quality boundary conditions to the LES, a relatively large outer domain with 900-m grid spacing was configured to downscale different reanalysis data (Fig. 1a). Inspired by the ensemble simulation approach demonstrated in Rasmussen et al. (2018) and encouraged by the wealth of good quality observational data collected in this case, we conducted 900-m simulations using four different reanalysis datasets [the Climate Forecast System, version 2 (CFS2); North American Regional Reanalysis (NARR); ECMWF interim reanalysis (ERA-Interim); and fifth major global reanalysis produced by ECMWF (ERA5)] and tested cloud condensation nuclei (CCN) concentrations, ice nucleating particle

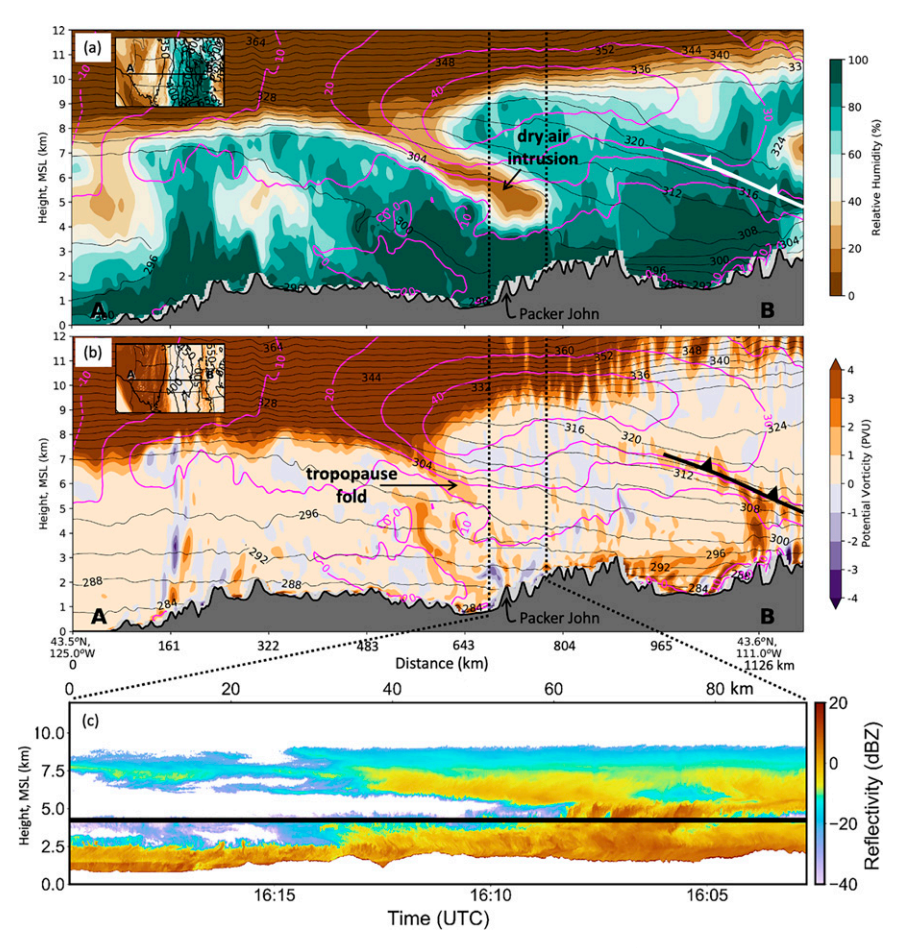


FIG. 3. Cross section of meridional wind (magenta contours; m s⁻¹) at 1600 UTC 19 Jan 2017 along a zonal line from the West Coast to western Wyoming (shown on the insert maps and in Fig. 2), overlain on (a) relative humidity with respect to water (%) and (b) potential vorticity (PV units, or PVU; 1 PVU = 10^{-6} K kg⁻¹ m² s⁻¹). The thin black contours are θ_e in (a) and θ in (b) (K). (c) An ~1/10-as-long transect of equivalent radar reflectivity measured by the W-band Wyoming Cloud radar during the flight leg between 1603 and 1620 UTC 19 Jan 2017.

(INP) concentrations, and planetary boundary layer (PBL) physics sensitivity to identify the most representative forcing to drive the LES runs. The simulation based on validation of cloud structure and supercooled liquid water properties was used to generate initial and boundary conditions every 10 min for the 300- and 100-m LES runs using the WRF one-waynest downscaling capability.

For all domains, 81 terrain-following, vertically stretched levels from the surface to 20 hPa, with 23 levels in the lowest 1000 m and 43 levels in the lowest 3000 m above ground level (AGL) were used. The high vertical resolution was designed to capture the orographic cloud top and the AgI dispersion around the cloud-top height. The Noah Multiphysics (MP) land surface model (Niu et al. 2011), Rapid Radiative Transfer Model for GCMs (RRTMG) radiation scheme (Pincus et al. 2003) and the Thompson–Eidhammer scheme (Thompson and Eidhammer 2014) with the updated cloud seeding parameterization (Rauber et al. 2019) were used for all simulations. The use of the Mellor–Yamada–Nakanishi–Niino (MYNN;

Nakanishi and Niino 2004, 2006) and Yonsei University (YSU; Hong et al. 2006) PBL schemes and different CCN and INP initial conditions were tested in 900-m simulations. The details of the final model configuration from this optimization are listed in Table 1.

To assess airborne AgI seeding impacts on clouds and precipitation in SNOWIE IOP5, simulations without seeding served as the control runs (CTRL) and simulations including airborne seeding served as the seeding runs (SEED). The differences in cloud and precipitation fields between the corresponding CTRL and SEED simulations indicate the simulated seeding impacts on clouds and precipitation.

Two distinct seeding lines (enhanced DOW reflectivity fields) that corresponded to the first two seeding legs were observed during this IOP (French et al. 2018; Friedrich et al. 2020). In our SEED simulations, two moving point sources of AgI were implemented to represent the first two seeding legs matching the timing, locations and released rate of the AgI from the burned-in-place flares (Friedrich et al. 2020).

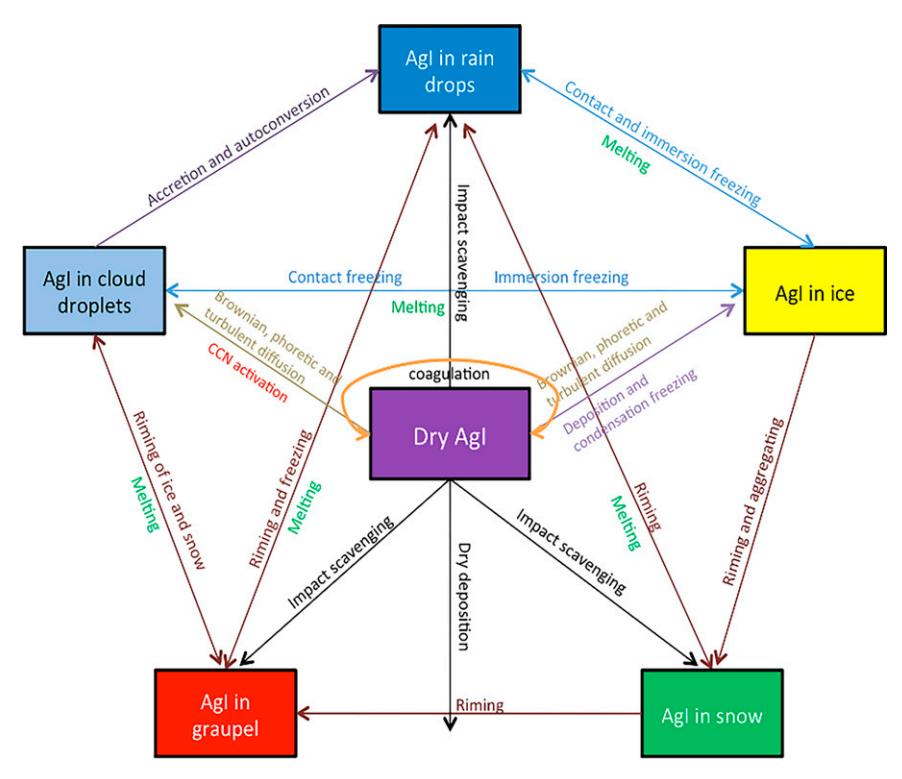


FIG. 4. Schematic of the AgI–cloud interactions that are simulated in the seeding parameterization [adapted from Fig. 7 in Rauber et al. (2019)].

Table 2 lists all of the simulations discussed in this study. The experiment names start with the grid spacing followed by the name of the reanalysis data. As seen in Table 1, CCN, INP, PBL physics, boundary conditions, and AgI activation rate are perturbed to compare with observations. The default background CCN concentration is the default Goddard Chemistry Aerosol Radiation and Transport (GOCART) 7-yr monthly climatology for the Thompson–Eidhammer scheme while "03CCN" represents the simulations using 30% of the background aerosol concentration climatology. The "DeMott2010" default ice nucleation parameterization (DeMott et al. 2010) was used for most of the experiments, while "MEYERS" indicates the simulation applying the Meyers ice nucleation parameterization

(Meyers et al. 1992). The MYNN scheme was picked as the default PBL physics based on our testing. Experiments with "YSU" either used the YSU scheme (900-m simulations) or had the boundary conditions generated by simulation using YSU scheme (300- and 100-m LES runs). For some of the LES runs, the wind boundary conditions were replaced by those generated from the 900-m run driven by ERA-Interim data. Last, a set of SEED experiments was conducted using 5 times the default AgI nucleation rate (names with "5X") to test the seeding sensitivity. All these sensitivity tests were consistent with the ensemble design in Rasmussen et al. (2018) to address some of the important uncertainties associated with the natural and seeded cloud/precipitation processes.

TABLE 1. Model configurations.

	900-m non-LES	300-m LES	100-m LES	
Horizontal grids	900 × 600	540 × 540	1200 × 1200	
Time step	5 s ¹ / ₃ s		1/9 s	
Driving data	CFS2/NARR/ERA-I/ERA5 reanalysis	Interpolation from 900-m results (ERA5)		
Simulation time	0000–1900 UTC 19 Jan 2017	1500–1820 UTC 19 Jan 2017		
Vertical coordinate	81 terrain-following ETA levels			
Land surface model	Noah MP			
Radiation	RRTMG longwave and shortwave			
PBL scheme	MYNN 2.5 order/YSU	_		
Microphysics	Thompson-Eidhammer with cloud seeding parameterization			
CCN and IN tests	CCN/IN		_	
Boundary conditions	_	ERA5/ERA-I wind	_	
AgI nucleation rates	Regular	Regular/5×	Regular/5×	

TABLE 2. List of numerical experiments. Boldface type emphasizes how a particular configuration differs from previous ones.

CTRL	SEED	Driving data	Configurations
900m_CFS2_CTRL	_	CFS2	CCN climatology; DeMott2010 INP; MYNN PBL
900m_NARR_CTRL	_	NARR	CCN climatology; DeMott2010 INP; MYNN PBL
900m_ERAI_CTRL	_	ERA-Interim	CCN climatology; DeMott2010 INP; MYNN PBL
900m_ERA5_CTRL	900m_ERA5_SEED	ERA5	CCN climatology; DeMott2010 INP; MYNN PBL
900m_03CCN_CTRL	900m_03CCN_SEED	ERA5	30% CCN climatology; DeMott2010 INP; MYNN PBL
900m_MEYERS_CTRL	900m_MEYERS_SEED	ERA5	30% CCN climatology; Meyers INP; MYNN PBL
900m_YSU_CTRL	900m_YSU_SEED	ERA5	30% CCN climatology; DeMott2010 INP; YSU PBL
300m_ORI_CTRL	300m_ORI_SEED	900m_YSU_CTRL	DeMott2010 INP; input data are interpolated from
		output	900m_YSU_CTRL outputs; "ORI" means the original wind field from 900m_YSU_CTRL
300m_CTRL	300m_SEED and 300m_SEED_5X	900m_YSU_CTRL output + 900m ERAI CTRL	DeMott2010 INP, input data are interpolated from 900m_YSU_CTRL outputs; wind tendencies are interpolated from 900m_ERAI_CTRL outputs
		output	
100m_CTRL	100m_SEED and 100m_SEED_5X		Nested within 300m _CTRL

4. Results

a. Comparisons of environments and cloud structure

Cloud and precipitation properties are largely determined by the environmental conditions. Previous limited-area numerical studies also showed that simulated clouds and precipitation are very sensitive to the driving data (Kala et al. 2015; Rasmussen et al. 2018). Therefore, we ran IOP5 with four commonly used reanalysis datasets, which are CFS2 (Saha et al. 2014), NARR (Mesinger et al. 2006), ERA-Interim (Dee et al. 2011), and ERA5 (Hersbach et al. 2020). CFS2 and ERA-Interim provide 6-hourly boundary conditions in ~0.5° by 0.5° and 0.75° by 0.75° resolution, respectively. NARR provides 3-hourly data in ~30 km by 30 km resolution. ERA5 data are the newest reanalysis product from the ECMWF that provides hourly data in ~0.25° by 0.25° resolution. With 15 h of spinup time, all 900-m simulations driven by these datasets generated well-balanced atmospheric conditions and produced orographic clouds over the SNOWIE campaign area.

Figure 5 shows comparisons of different environmental parameter profiles from Crouch ("CR +" in Fig. 1b) between observations and 900-m simulations (900m_CFS2_CTRL, 900m_ERA5_CTRL, 900m_ERA1_CTRL, and 900m_NARR_CTRL) at 1625 UTC. These simulations reasonably captured the observed temperature profile below 4 km. We attribute the superadiabatic lapse rate around 5 km in the observations to evaporative/sublimational cooling of the condensate on the temperature sensor (Hodge 1956; Slonaker et al. 1996) after the sounding entered the dry-air intrusion above the lower orographic cloud (black line in Fig. 5b). The 900m_ERAI_CTRL produced a neutral to slightly unstable condition between 1 and 5 km. All other simulations generated stable conditions in this layer.

The dry-air intrusion formed a very sharp relative humidity (RH) gradient between 4.5 and 5 km (Fig. 5c). All simulations had difficulties reproducing the sharp gradient but ERA5 and ERAI are able to simulate much dryer conditions in this layer

than CFS2 and NARR (Fig. 5c). ERAI captured the wind speed and direction through the entire atmosphere well in comparison with observations. The rest of the simulations underpredicted the wind speed between 2 and 3.5 km. ERA5 and NARR also produced more southerly wind (~30°) between 1 and 3 km.

The cloud structures observed by the UWKA WCR between 1622 and 1636 and the simulated cloud structures in four 900-m control runs at 1625 UTC are shown in Fig. 6. The Cloud-Resolving Model Radar Simulator (CR-SIM; Oue et al. 2020) is used to reproduce reflectivity factor from the simulation results. The emulated radar is specified as a vertically scanning W-band radar at the average UWKA flight level with a beamwidth of 0.3°. To obtain a more realistic comparison with the observations, attenuation is integrated from the flight level to the bottom and top of the model, respectively. The WCR reflectivity field shows two cloud layers with the gap between the layers decreasing from west to east (Fig. 6a). All simulations produce a double-layer cloud structure in some areas of the cross section. NARR run fails to simulate the high reflectivity in the upper cloud (Fig. 6e). Likely due to the neutral to slightly unstable condition in the low atmosphere (Fig. 5b), the ERAI run simulates a broken orographic cloud with many convective cloud elements (Fig. 6d). The weaker dry-air intrusion simulated by CFS2 run makes the cloud base of the upper layer cloud lower than what the WCR reflectivity shows (Fig. 6b).

Regardless of different cloud structures, all runs simulate supercooled liquid cloud tops and freezing drizzle (appendix Fig. A2). The cloud-top temperature of the orographic cloud is $\sim -15^{\circ}\text{C}$ in CFS2 and ERA5 runs, which is in good agreement with the observed value (not shown). The cloud-top temperature is from -20° to -15°C in the NARR and ERAI simulations (appendix Fig. A2). The irregular cloud-top height in the ERAI run is a reflection of the convective nature of the environments.

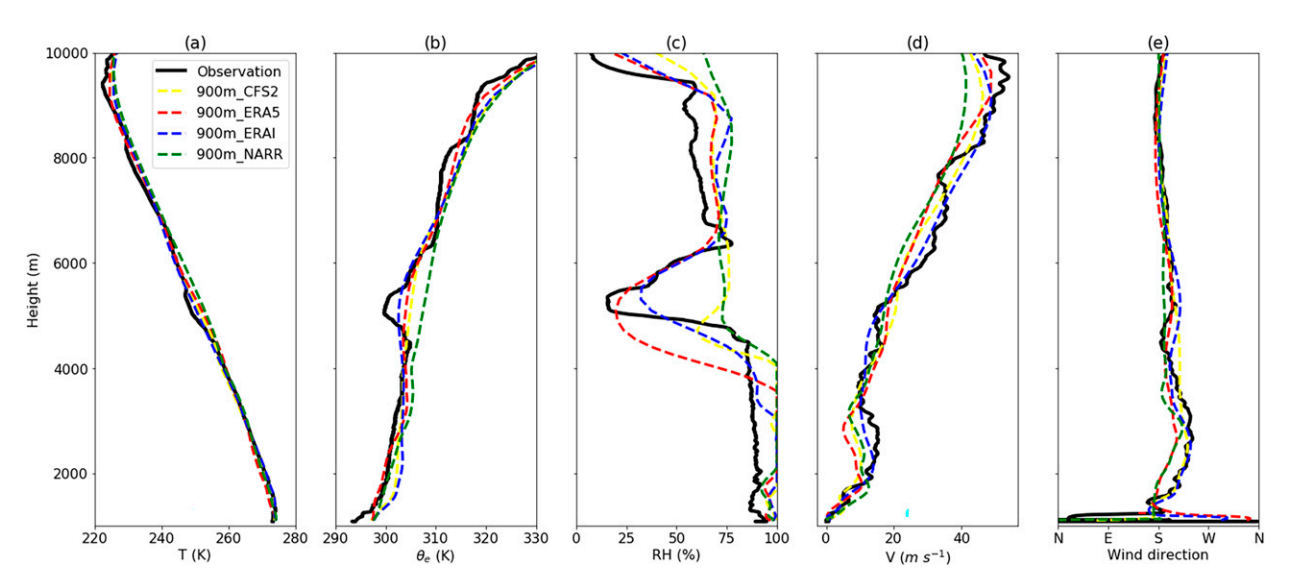


FIG. 5. Observed and simulated profiles from Crouch at 1625 UTC. Black represents observations, and colored dashed lines indicate results from 900-m simulations driven by different reanalysis data (yellow for CFS2, red for ERA5, blue for ERAI, and green for NARR). The parameters are (a) temperature (K), (b) equivalent potential temperature (K), (c) relative humidity (%), (d) wind speed (m s⁻¹), and (e) wind direction.

The sounding and cloud structure comparisons indicate that the simulation driven by the ERA5 reanalysis captures the macro properties of the case better than the runs driven by other reanalysis datasets.

b. Comparisons of cloud supercooled liquid water

Correct simulation of supercooled liquid water is critical to get right for glaciogenic seeding. Figure 7 shows the box-andwhisker plots of the cloud droplet concentration (CDC) and cloud liquid water content (CLWC) from both observations and model results. The observations are from the cloud droplet probe (CDP) measurements along all 10 UWKA flight legs. Since some observations were influenced by seeding, the seeding simulation results were interpolated along the track in space and time to compare with observations. For the three legs that observations were collected before seeding started, the model results from the control runs were analyzed. For the observations, only the data when 2DS particle concentrations $< 0.5 L^{-1}$ and CDP concentrations $> 3 cm^{-3}$ are included in the analysis. Therefore, model data with ice water content < 0.05 g m⁻³ (roughly corresponding to concentration $< 0.5 L^{-1}$ for ice-phase particles $> 100 \mu m$) and CDC > 3 cm^{-3} are used.

Observed cloud droplet concentrations during SNOWIE were low (Tessendorf et al. 2019; Majewski and French 2020). It is clear that the CCN concentration climatology overpredicted the observed cloud droplet concentration (900m_ERA5_SEED in Fig. 7a). A scaled-down CCN concentration of 30% of the CCN climatology reproduced well the observed CDC along the UWKA tracks (900m_03CCN_SEED in Fig. 7a). The INP concentration and PBL physics do not impact the CDC distributions much (900m_MEYERS_SEED and 900m_YSU_SEED in Fig. 7a). The interquartile range is smaller and the median

value is slightly higher in these simulations relative to the observations.

The CCN climatology produced a higher median CLWC value (0.2 g m⁻³) and a broader range than other simulations and observations. Lower CCN concentrations reduced the median CLWC to 0.15 g m⁻³ (Fig. 7b). The CLWC distribution from the Meyers INP parameterization simulation agreed well with the observed values (Fig. 7b). The 900m_YSU_SEED results are slightly improved relative to the 900m_03CCN_SEED results (Fig. 7b). The observations included data around the cloud edges and boundaries that were small in value and contributed to the low CLWC statistics due to the impacts of entrainment and detrainment processes. One possible reason of the high bias in CLWC is that the model resolution is not fine enough to resolve these mixing processes. Another possible reason is the difference in the thermodynamics and cloud structure between simulations and reality.

Figure 8 illustrates the time series of the observed and simulated LWP. The black dashed sections indicate the periods when rain wetted the radome, making the measurements more uncertain. The model data is calculated along the same path direction as the radiometer (southerly at 15° elevation from the horizon). The radiometer measurements showed that the supercooled liquid water persisted in the seeding area throughout the IOP with an averaged LWP around 0.3 mm. All simulations underpredicted the LWP before 1600 UTC while 900m_MEYERS_SEED underestimated the LWP throughout the simulation period. The other simulations captured the LWP trend well after 1710 UTC except for slightly underestimated values from 900m_ERA5_SEED and 900m_03CCN_SEED. The simulation with the YSU PBL agrees with observations the best in terms of LWP evolution and magnitude. When the grid spacing is refined to 300 and 100 m, the LWP is above the observed value, which may impact the simulated seeding effects on clouds (not shown).

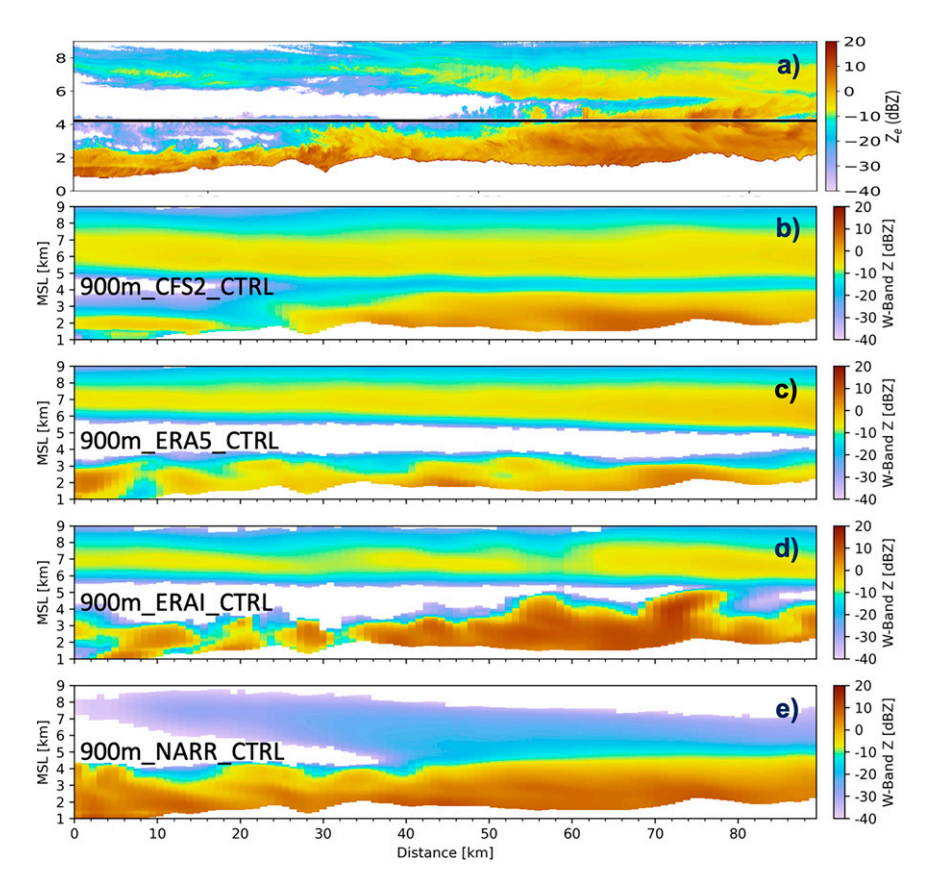


FIG. 6. (a) UWKA observed WCR reflectivity field during leg 3 from 1622 to 1636 UTC, and the corresponding model-based cross sections at 1625 UTC for (b) 900m_CFS2_CTRL, (c) 900m_ERA5_CTRL, (d) 900m_ERAI_CTRL, and (e) 900m_NARR_CTRL. Model results are converted to W-band radar reflectivity fields using CR-SIM.

The comparisons of cloud supercooled liquid water properties indicate that the 900-m simulation driven by ERA5 data using a lower CCN concentration (30% of the climatology) and the YSU PBL scheme is able to reproduce the observed cloud structure and properties best.

c. Comparisons of seeding impacts on cloud

To further compare the observed and simulated seeding impacts and explore the role of model grid spacing, results from 900m_YSU_SEED (Table 2) and from LES seeding simulations with 300- and 100-m grid spacing (including 300m_ORI_SEED, 300m_SEED, 300m_SEED, 3100m_SEED, and 100m_SEED_5X) are analyzed in this section.

Figure 9 shows the comparisons of seeding plume morphology and position at 1730 UTC between model results and observations from the DOW at Snowbank. This time is centered on the period that seeding effects were analyzed in Friedrich et al. (2020) (from 1640 to 1820 UTC). The red outline represents the contour of 20 dBZ of the quality-controlled composite DOW reflectivity (Friedrich et al. 2020). The black contours representing the model seeding plumes are defined by the simulated snow mixing ratio $> 0.02 \text{ g kg}^{-1}$ (minimum observed value within the WCR-determined seeding

plumes) and simulated AgI particle concentration $> 1 L^{-1}$ at 3700 m MSL (the averaged UWKA flight height).

The simulated seeding plumes are much wider and broader in 900m_YSU_SEED than in 300m_ORI_SEED (Figs. 9a,b). The 900-m simulation could not distinguish two individual seeding lines as observed by the DOW. The 300m_ORI_SEED run captured the overall width of the seeding plumes and simulated two separate seeding lines. Although the simulated seeding plumes of these two runs have the same orientation as the observed plumes, they are displaced northwest relative to the observed signals. This displacement is caused by the stronger southerly wind component relative to the observed wind field in the ERA5 data (Fig. 5e). To improve the simulated seeding impact on clouds and precipitation, the lateral boundary conditions of wind tendencies for the 300- and 300-100-m nested LES runs were replaced with those generated from 900m_ERAI_CTRL run. The sounding comparisons between the LES runs with and without the updated wind and observations indicate that both the simulated wind speed and direction are improved by the updated wind (appendix Fig. A1).

As a result of the better representation of the wind field, 300m_SEED and 100m_SEED simulated seeding plumes are in similar positions to the observed ones (Figs. 9c,e). Both

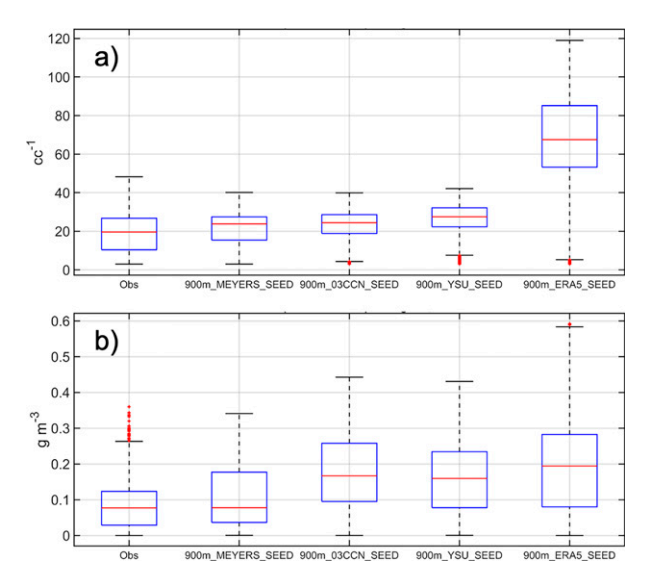


FIG. 7. Box-and-whisker plots of (a) the cloud droplet concentration (cm⁻³) and (b) liquid water contents (g m⁻³) for observations and model results. All data are from the "in cloud" condition based on definitions of observations and model results (see the main text for details) and along all UWKA flight tracks.

simulations show a double line structure with 100_SEED producing more details than 300m_SEED. However, the linear structure in simulations is not as apparent as the observed plumes due to more variabilities in the simulated wind field and cloud liquid water field. Increasing the AgI nucleation rate by 5 times (300m_SEED_5X and 100m_SEED_5X) led to broader seeding plumes relative to 300m_SEED and 100m_SEED (Figs. 9d.f).

Similar analyses were performed at different levels (from 3500 to 4000 m MSL), at different model output times (from 1640 to 1820 UTC), and with a different snow mixing ratio threshold (0.1 g kg⁻¹) (not shown). In general, the simulated seeding plumes are narrower and more distinguishable at higher levels than lower levels due to the snow growth as particles descended through the cloud and more complicated wind fields close to the ground. The linear seeding plume

structure is more obvious at earlier times due to less dispersion of AgI particles closer to the source region than at later times. The seeding plumes are narrower and more broken when a larger snow mixing ratio threshold was used to define their boundaries. Overall, LES seeding simulations using the updated wind captured the general features of the observed seeding plumes.

Changing the wind field or nudging the mean wind toward the observed wind profile is a common strategy in many idealized simulations (driven by a single upstream sounding) on orographic clouds, squall lines, cloud generating cells, and many other cloud systems, for the purpose of investigating the sensitivity of simulated storm structure/organization, cloud properties and precipitation to the wind and shear (Xue et al. 2010, 2013a; Keeler et al. 2017; Atlas et al. 2020). This approach, however, is not common in real-case simulations. Chen et al. (2015) adjusted the lateral boundary conditions of the wind tendencies in a real convective system simulation, to examine the impact of the shear location on storm organization and precipitation. One consequence of changing the wind tendencies is that the vapor flux into the simulation domain changes. In our case, the time series of the vapor flux from the 300m_ORI_CTRL and 300m_CTRL (with updated wind tendencies) simulations into the 100-m LES domain (where seeding impacts occurred) are shown in Fig. 10. It shows that the 300m_CTRL took about 40 min to reach a new balance under the updated wind field due to the relatively small size of the 300-m domain. Between 1640 and 1820 UTC, when the seeding effects were observed, about 10% more vapor entered the 100-m LES domain in 300m_CTRL than 300m_ORI_CTRL. The additional vapor and changed wind fields increased the LWC and altered the precipitation magnitude and distribution over the target (not shown), which will be discussed later in the paper.

The observed and simulated vertical structures of the seeding plumes are compared in Fig. 11. Relative to observations, all simulations show stronger reflectivity upwind of the seeding plumes indicating possible influences of these upwind cloud hydrometeors on the seeding-impacted areas through advection. The UWKA WCR reflectivity cross section

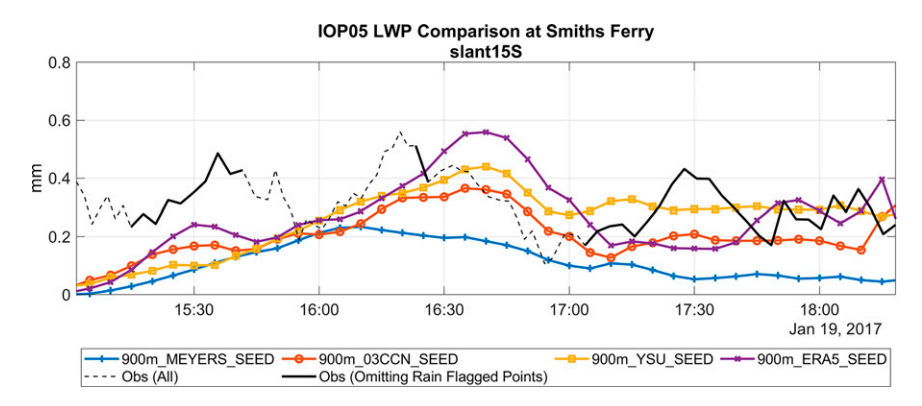


FIG. 8. Time series of the liquid water path for radiometer observations (black lines) and model results (colored lines) at Smiths Ferry. Model data are extracted along the actual radiometer beam toward south direction with an elevation angle of 15°.

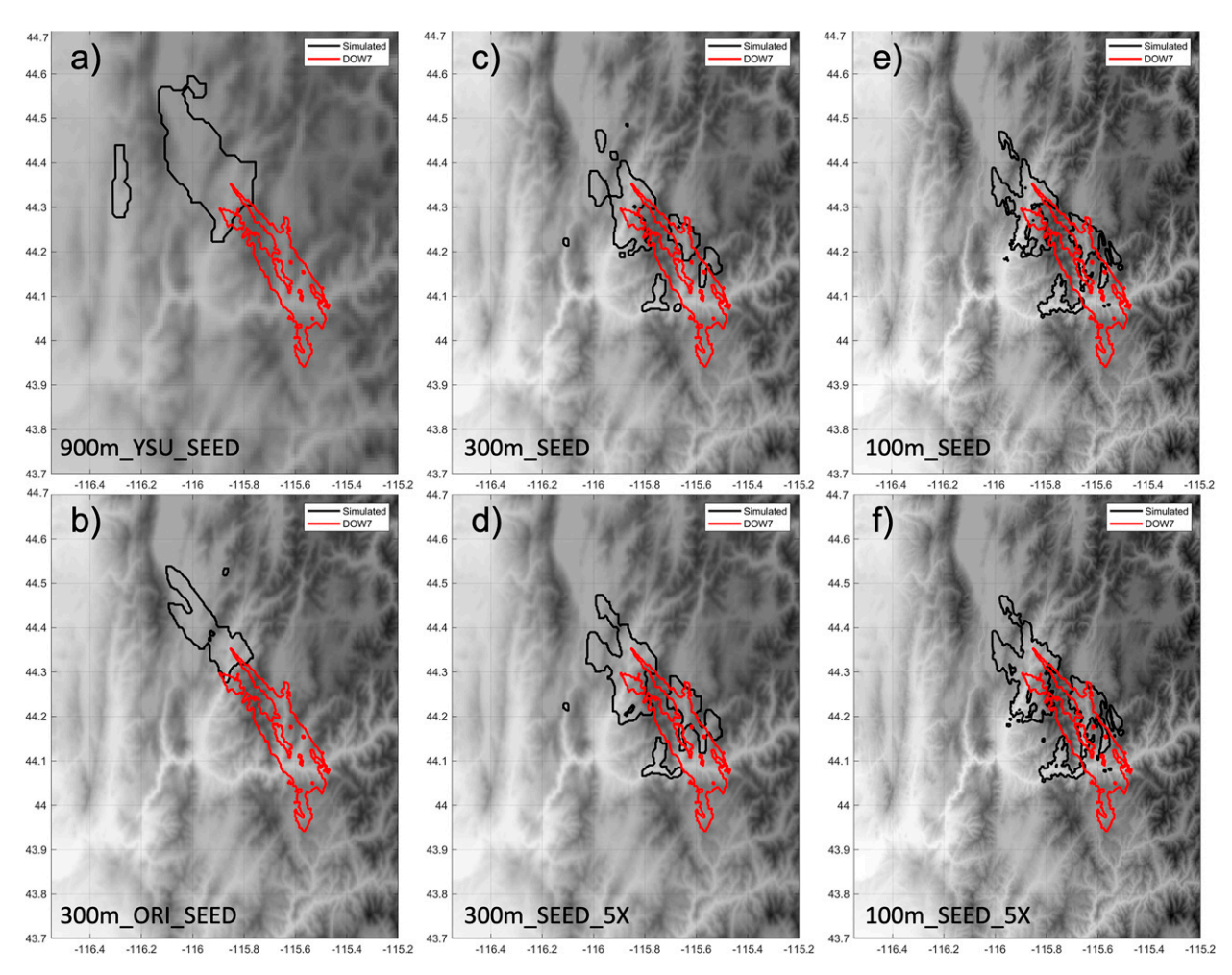


FIG. 9. The maps of DOW-derived seeding plume outline (red) and simulated seeding plume outline at 3700 m MSL (black) for simulations (a) 900m_YSU_SSED, (b) 300m_ORI_SEED, (c) 300m_SEED, (d) 300m_SEED_5X, (e) 100m_SEED, and (f) 100m_SEED_5X.

between 1725 and 1735 UTC shows two distinct high reflectivity regions (dBZ>0) corresponding to the seeding lines, with the eastern one being more vertically oriented than the western one (Fig. 11a). At flight level, each of these seeding plumes was about 5 km wide. There was only one broad and

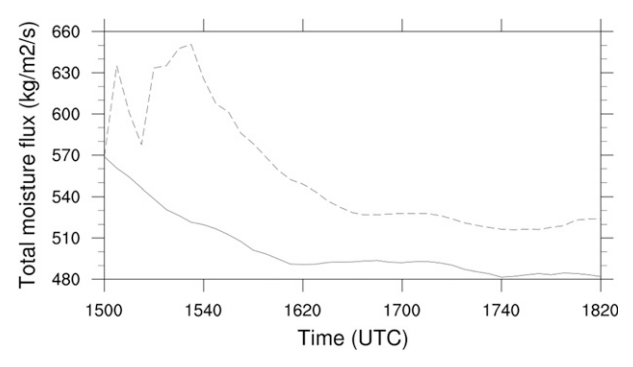


FIG. 10. Time series of the moisture flux entering the 100-m LES domain. The solid line represents the values from the 300m_ORI_CTRL run. The dashed line is for 300m_CTRL.

tilted seeding plume (high W-band reflectivity converted by CR-SIM) in the 900m_YSU_SEED simulation at 1730 UTC along the UWKA flight track (Fig. 11b). The single seeding plume is narrower in the 300m_ORI_SEED simulation (Fig. 11c). Both 300m_SEED_5X and 100m_SEED_5X simulated two separate seeding plumes of similar widths and at locations close to those observed (Figs. 11d,e). The tilted structure of the western plume due to wind shear was well captured in both LES runs especially in the 100m_SEED_5X. Neither simulation simulated the vertically oriented structure of the eastern plume. The simulated eastern seeding plume tilted the same way as the western one indicating stronger wind shear in the model than in observations at this location. The reflectivity below 3.5 km MSL is overestimated by all simulations indicating more active ice processes in the model. The AgI particles were dispersed over a larger volume in 900m_YSU_SEED relative to the other LES runs [purple contours in appendix Figs. A3(b)-A3(e)].

The UWKA in situ observations of LWC, CDC, ice water content (IWC) and temperature along flight leg 7 are compared with corresponding model results in Fig. 12. The model data

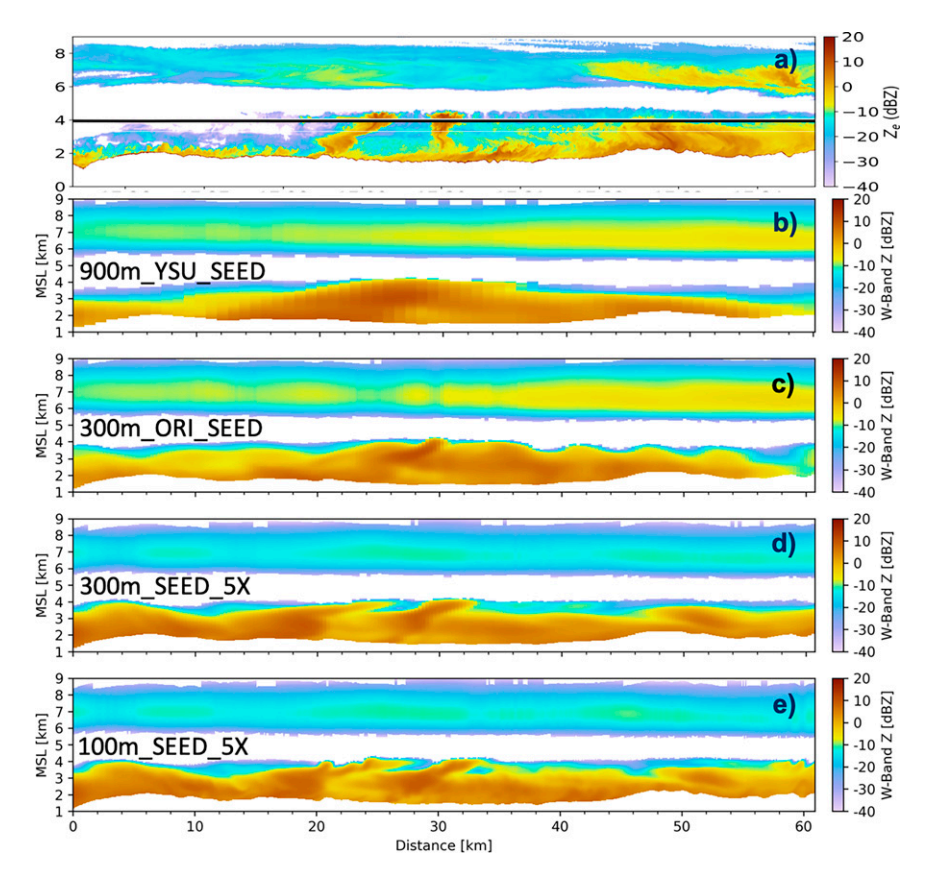


FIG. 11. As in Fig. 6, but for (a) UWKA WCR reflectivity during leg 7; (b) 900m_YSU_SEED, (c) 300m_ORI_SEED, (d) 300m_SEED_5X, and (e) 100m_SEED_5X at 1730 UTC.

were interpolated in the same way as in Fig. 7. The shaded segments indicate the seeding plumes defined by WCR reflectivity > 0 dBZ close to flight level and IWC > 0.02 g m⁻³ in observations (red) and by snow mixing ratio $> 0.02 \text{ g kg}^{-1}$ and AgI concentration $> 1 L^{-1}$ in model results (blue). The corresponding data from the control runs are plotted in black dotted lines. Similar to Fig. 11, more upwind liquid water contents were found upwind of the seeding plumes in all simulations relative to observations. The advection of such liquid water may lead to different seeding responses in simulations from the reality. The comparisons show that 900m_YSU_SEED and 300m_ORI_ SEED underestimated the LWC and CDC values downwind of the seeding plumes (Figs. 12a1, 12a2, 12b1, and 12b2). On the other hand, 300m_SEED_5X and 100m_SEED_5X slightly overestimated these fields (Figs. 12c1, 12c2, 12d1, and 12d2). The 900m_YSU_SEED and 300m_ORI_SEED simulated a single seeding plume wider than two observed plumes combined at the UWKA flight level, which is consistent with what Figs. 9 and 11 show. Both LES runs with updated wind simulated two separate seeding plumes with 100m_SEED_5X in better agreement with the observed plume widths and locations. A maximum of about 0.3 g m⁻³ LWC from the CTRL run was depleted in the seeding plumes for each simulation set (Figs. 12a1, 12b1, 12c1, and 12d1). However, due to the possible sedimentation of ice precipitating particles, the IWC only reaches about 0.1 g m⁻³ in the seeding plumes (Figs. 12a3, 12b3, 12c3, and 12d3). The higher IWC in observed seeding plumes implies a slower fall speed of the ice particles than the model. Both 300m_SEED_5X and 100m_SEED_5X runs showed a consistent cold bias at about 0.5°C due to cold-air advection by the updated winds and simulated temperature structure in better phase with observations than 900m_YSU_SEED and 300m_ORI_SEED runs (Figs. 12a4, 12b4, 12c4, 12d4).

The model-observation comparisons performed so far have shown that the WRF-WxMod simulations of the SNOWIE IOP5 case can reasonably simulate the cloud properties impacted by AgI seeding. To validate the AgI seeding parameterization within WRF-WxMod, the AgI nucleation rate should be evaluated. However, the AgI nucleation rate consisting of several AgI nucleation modes is a combined microphysical process that may be observable in a controlled laboratory environment but very difficult to measure in the field (Morrison et al. 2020). Therefore, we can only infer the accuracy or appropriateness of the AgI seeding parameterization by comparing the outcome of the AgI nucleation process in terms of ice number concentration inside the seeding plumes.

Because of the detection limitations and uncertainties of the UWKA in situ instruments, only particles with diameter greater than $100~\mu m$ can be confidently classified as ice-phase hydrometeors. The number concentrations of

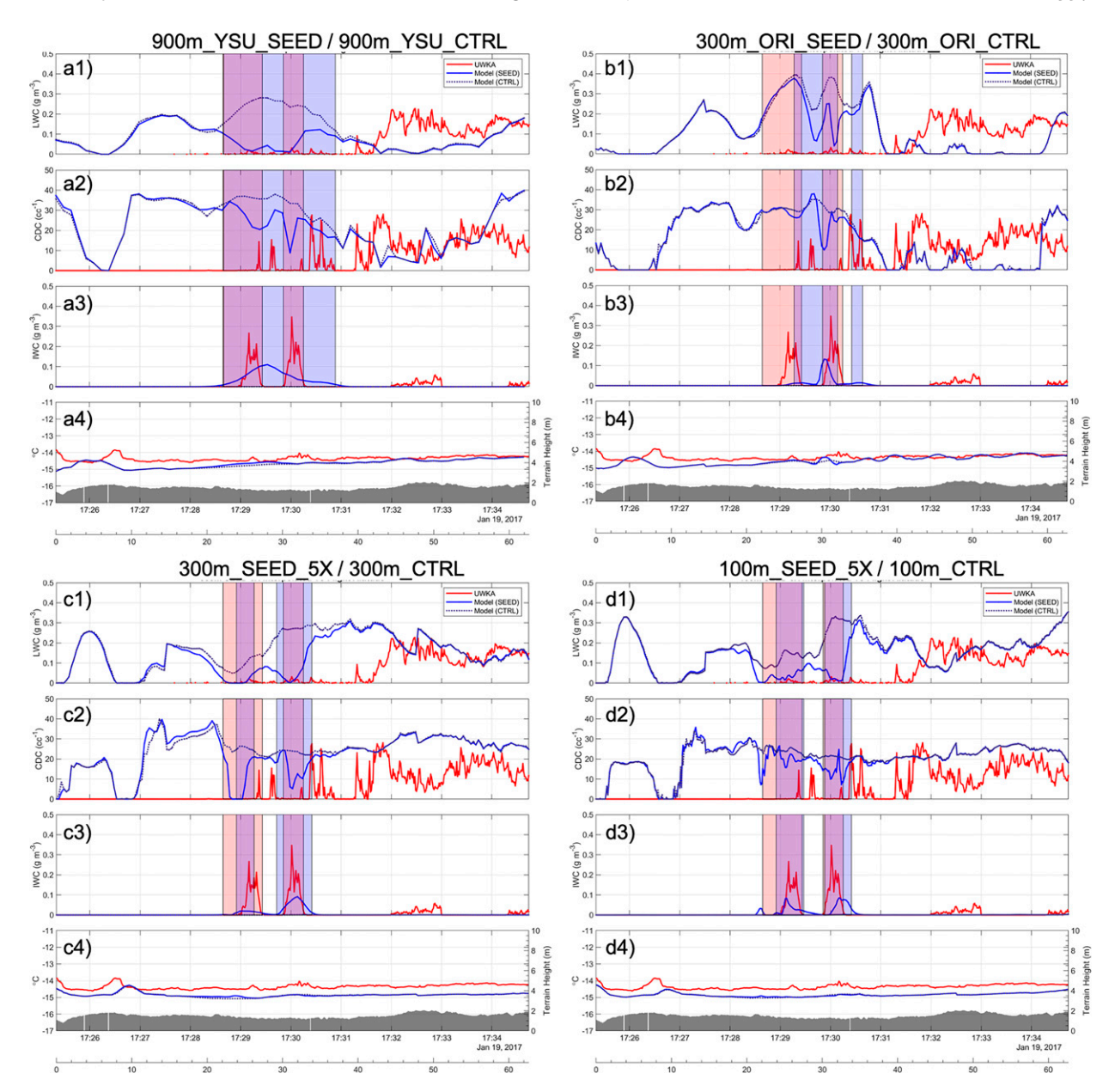


FIG. 12. (a1),(b1),(c1),(d1) Liquid water content; (a2),(b2),(c2),(d2) cloud droplet concentration; (a3),(b3),(c3),(d3) ice water content; and (a4),(b4),(c4),(d4) temperature along the UWKA flight track 7 from observations (red lines), model results from seeding simulations (blue solid lines), and model results from the corresponding control simulations (dark-blue dotted lines). The model data are shown for (top left) 900m_YSU_SEED and 900m_YSU_CTRL, (top right) 300m_ORI_SEED and 300m_ORI_CTRL, (bottom left) 300m_SEED_5X and 300m_CTRL, and (bottom right) 100m_SEED_5X and 100m_CTRL. The shaded areas indicate the seeding plumes. The topography underneath the UWKA is also plotted in gray in all temperature panels for reference.

particles greater than $100~\mu m$ (PNC100) based on data from both the 2D-S and 2DP are computed and averaged within the seeding plumes for each flight leg and are compared with the model counterparts in a scatterplot (Fig. 13). For the model data, the size distributions of all hydrometeor species are backed out from the simulated mass and number mixing ratios based on the assumed PSD functional forms (Thompson et al. 2008; Thompson and Eidhammer 2014) within the simulated seeding plumes. The PNC100 based on

the combined PSD were calculated and averaged within the seeding plumes for each flight leg. Since data from seeding plumes are only available from legs 4–10, seven data points of PNC100 in the unit of inverse liters were included for each simulation in Fig. 13.

The results show that 900m_YSU_SEED overestimated the PNC100 in 4 of 7 legs. 300m_ORI_SEED, 300m_SEED and 100m_SEED underestimated the PNC100 in 5 legs. 300m_ORI_SEED (100m_SEED) simulated lower PNC100 than 900m_

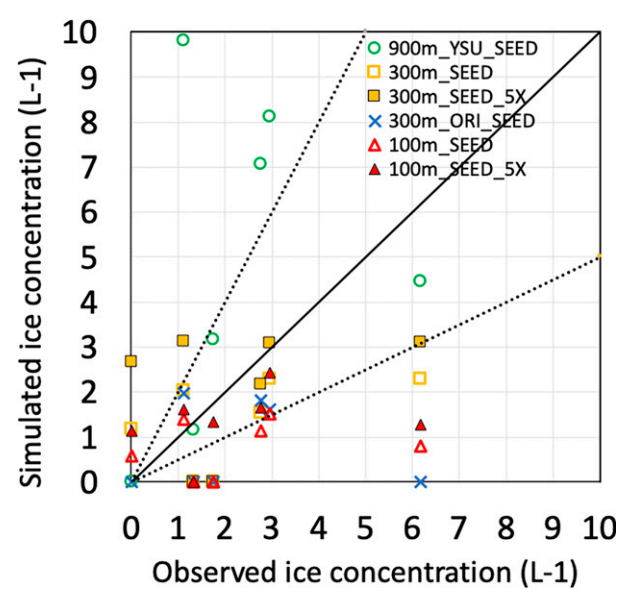


FIG. 13. Scatterplots between observed and simulated particle concentrations with diameter greater than 100 μ m inside the seeding plumes. Each symbol represents the average concentration of one UWKA flight leg.

YSU_SEED (300_SEED) in each leg. When the AgI nucleation rate was increased by 5 times, the simulated PNC100 were in better agreement with the observed values (more data points from 300m_SEED_5X and 100m_SEED_5X runs were within a factor of 2 indicated by black dashed lines). The averaged PNC100 value inside seeding plumes over 7 legs is 2.7 (observation), 5.6 (900m_YSU_SEED), 0.8 (300m_ORI_SEED), 1.9 (300m_SEED), 2.8 (300m_SEED_5X), 1.1 (100m_SEED), and 1.6 (100m_SEED_5X) L⁻¹. The simulated seeding effects on precipitation is positively correlated with the averaged PNC100 (Table 3). Note that, although the PNC100 values were small inside the seeding plumes, the simulated ice number concentrations over the entire size range were much larger. The maximum ice number concentration values representing the center of the seeding plumes range from 200 to 820 L⁻¹ among these seeding simulations.

To explain the different magnitudes of PNC100 simulated by different experiments, the AgI dispersion volume and the total ice number in the cloud-top region (3750-4250 m MSL) within the 100-m LES domain are analyzed (Fig. 14). Figure 14a shows that the volume of AgI particle dispersion (volume of the AgI concentration >0) is correlated with the grid spacing. In 900m_YSU_SEED, the AgI particles were dispersed into a larger volume in the cloud-top region in agreement with Figs. 9 and 11, which results in more nucleated ice particles (Figs. 13 and 14b). When the grid spacing is reduced, the numerical diffusion reduces too, resulting in smaller volumes of AgI dispersion. The AgI moved out of the 100-m LES domain after 1740 UTC in 900m_YSU_SEED and 300m_ORI_SEED due to stronger southerly wind. AgI particles stayed in the domain longer in 300m_SEED and 300m_SEED_5X and dispersed into larger volumes than in 300_ORI_SEED. The enhanced AgI nucleation rate did not impact the AgI dispersion so that the AgI dispersion volume stayed the same in the 300m SEED and 300m_SEED_5X simulations, and in the 100m_SEED and 100m_SEED_5X runs, respectively. As a result of the different dispersion features, the total ice number in the cloud-top region scales with the grid spacing under the default AgI nucleation rate (Fig. 14b). Due to the different wind fields, the total ice number time series are different in 300m_ORI_SEED and 300m_SEED. When the AgI nucleation rate was increased (5X simulations), the total ice number increased accordingly. The general features of the total ice number in the cloud-top region agree with what Fig. 13 shows, indicating that seeding impacts on cloud and precipitation are sensitive to the grid spacing.

d. Comparisons of seeding impacts on precipitation

The seeding simulations showed similar vertical structures of seeding plumes to observations (Fig. 11), indicating that the seeding-induced snow reached the ground. The simulated natural precipitation and seeding effects on precipitation between 1640 and 1820 UTC (the observed seeding signal window) within the 100-m domain are shown in Fig. 15. Figures 15a1 and 15b1 show that the 300m_ORI_CTRL run produced slightly more precipitation and a stronger terrain influence on precipitation than the 900m_YSU_CTRL due to its better-resolved terrain–flow interactions. The 300m_CTRL

TABLE 3. Natural precipitation, seeding effects, and seeding-impacted areas for observations and all seeding simulations within the DOW range and 100-m domain during the period from 1640 to 1810 UTC.

Case	CTRL precipitation (af/kg)	Seeding effect (af/kg)	Seeding effect (%)	Seeding-impacted areas (km ²)
Observations	_	$64-157/0.79-1.94 \times 10^8$	_	2327
900m_ERA5_SEED	$3628/4.48 \times 10^9$	$330.6/4.08 \times 10^8$	9.1	3153
900m_03CCN_SEED	$4070/5.02 \times 10^9$	$191.5/2.36 \times 10^8$	4.7	2845
900m_MEYERS_SEED	$4795/5.91 \times 10^9$	$64.9/0.80 \times 10^8$	1.4	1716
900m_YSU_SEED	$3104/3.83 \times 10^9$	$244.3/3.01 \times 10^8$	7.9	2741
300m_ORI_SEED	$3467/4.28 \times 10^9$	$81.5/1.01 \times 10^8$	2.4	1840
300m_SEED	$6523/8.05 \times 10^9$	$120.0/1.48 \times 10^8$	1.8	2156
300m_SEED_5X	$6523/8.05 \times 10^9$	$182.0/2.24 \times 10^8$	2.8	2568
100m_SEED	$6631/8.18 \times 10^9$	$101.8/1.26 \times 10^8$	1.5	2109
100m_SEED_5X	$6631/8.18 \times 10^9$	$159.2/1.96 \times 10^8$	2.5	2489
Model mean	$5041/6.22 \times 10^9$	$164.0/2.02 \times 10^8$	3.8	2402

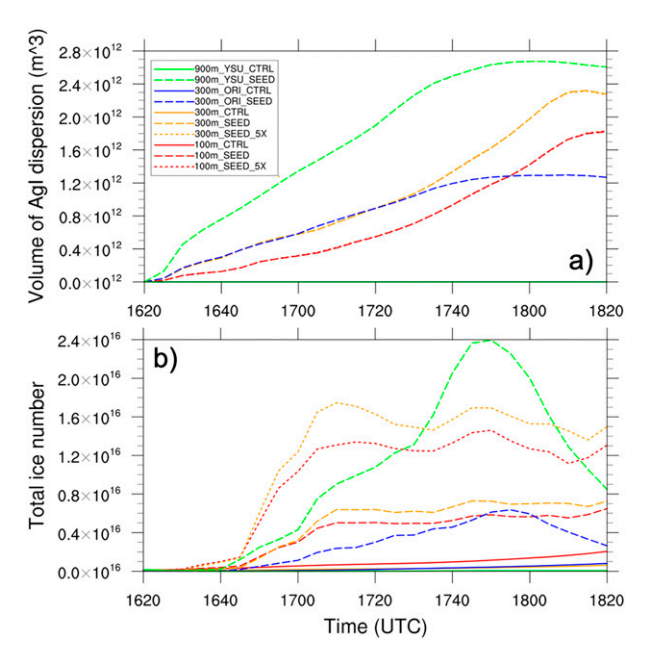


FIG. 14. Time series of the (a) AgI dispersion volume and (b) total number of ice particles within the cloud-top region for different seeding simulations.

generated a wider precipitation distribution with higher magnitude than 300m_ORI_CTRL, because of the changed wind field and stronger vapor influx (Figs. 15b1 and 15c1). In this case, a further refinement of grid spacing to 100 m changed the natural precipitation little in comparison with the 300-m simulation (Figs. 15c1 and 15d1).

The simulated seeding impacts on precipitation (precipitation difference between SEED and CTRL simulations) are located in the northwest region of the target basin in 900m_YSU_ SEED and 300m ORI SEED simulations due to the more southerly wind in these runs (Figs. 15a2 and 15b2). Because of the broader dispersed area and more nucleated AgI particles (Figs. 9, 13, and 14), 900m_YSU_SEED produced stronger precipitation enhancement in a wider area than 300m_ORI_ SEED. Simulated seeding effects are mostly within the target attributed to the more realistic wind direction in 300m_SEED (300m_SEED_5X) and 100m_SEED (100m_SEED_5X) runs (Figs. 15c2, 15c3, 15d2, and 15d3), which is in good agreement with the observed seeding-impacted region derived from the DOW reflectivity (Fig. 3A in Friedrich et al. 2020). The spatial distributions of seeding effects are very similar among these simulations with 100-m LES runs producing slightly weaker effects than the 300-m counterparts. When the AgI nucleation rate was increased, the seeding-impacted area and seeding enhanced precipitation both increased. In general, the features of the seeding effect distributions and magnitudes are in positive relation with the PNC100 (Fig. 13) and the cloud-top ice number concentration (Fig. 14).

The comparisons of the precipitation time series at three high-resolution snow gauge sites over the same period as Fig. 14 between observations and seeding simulations are presented in Figs. 16a1–d3. The model data within a square of 8.1

by 8.1 km² centered at the grid point that is closest to the gauge site (defined as the site area) were used to represent the spatial uncertainties of simulated precipitation relative to the observations. The size was chosen to represent the mean distance uncertainties associated with modeled precipitation trajectories based on our ongoing research (K. Heimes et al. 2021, manuscript submitted to J. Appl. Meteor. Climatol.). The precipitation evolution at the Silver Creek site (SC square in Fig. 1b) was well simulated by all seeding runs in terms of the mean values within the site area (Figs. 16a1, 16b1, 16c1, and 16d1). 900m_YSU_SEED simulated a narrow precipitation spread (Fig. 16a1). An increase of model resolution (300m_ORI_SEED) does not change the spread (Fig. 16b1). When the wind field is updated, the precipitation spread broadens at 300-m grid spacing (Fig. 16c1) and 100m_SEED_5X simulated a slightly wider precipitation spread than 300m_SEED_5X (Fig. 16d1). Relatively obvious seeding effects were generated at Silver Creek (0.04 to 0.18 mm) starting from 1730 UTC (Fig. 16e1). The time that the simulated seeding effect appeared at the site agreed well with the estimated times based on DOW observations (Fig. 2 in Friedrich et al. 2020).

Over Five Corners (south) and Banner Summit (east) sites, all seeding simulations underestimated the precipitation during this period (Figs. 16a2-d3). However, the means were closer to gauge data and the spread in the data covers the observed evolution in the simulations with updated wind fields. 300m_ORI_SEED simulated a wider spread than 900m_ORI_SEED only at Five Corners (Fig. 16b2). The spreads in the data were similar between 300m_SEED_5X and 100m_SEED_5X and much wider than those in 900m_YSU_SEED and 300m_ORI_SEED. No seeding effect was produced in 900m_YSU_SEED and 300m_ORI_SEED runs, due to the more southerly wind condition (Figs. 16e2 and 16e3). Small seeding effects (less than 0.02 mm) were found in 300m_SEED_5X and 100m_SEED_5X over these sites. The times of the appearance of seeding effect were also in line with the times derived from observations (Fig. 2 in Friedrich et al. 2020).

The comparisons of precipitation at three snow gauge sites indicate that the natural precipitation may be underestimated in all seeding simulations. Seeding runs with updated wind fields not only simulated natural precipitation evolution in better agreement with observations but also captured the right timings of the appearance of seeding effects. The simulated precipitation spatial variability is sensitive to wind conditions and grid spacing (degree of the resolved topography) depending on the location. The relative relationships of simulated seeding effects among these simulations are different than those from Fig. 15 mostly because the spatial coverages of the 900m_YSU_SEED and 300m_ORI_SEED seeding effects are very different from 300m_SEED_5X and 100m_SEED_5X and the three gauge sites are mostly within the seeding-impacted areas associated with the latter simulations.

The quantitative results of the natural precipitation and seeding effects in the unit of acre-feet (af; 1 af = 1233.5 m³) and in total mass (kg) are listed in Table 3 for all seeding

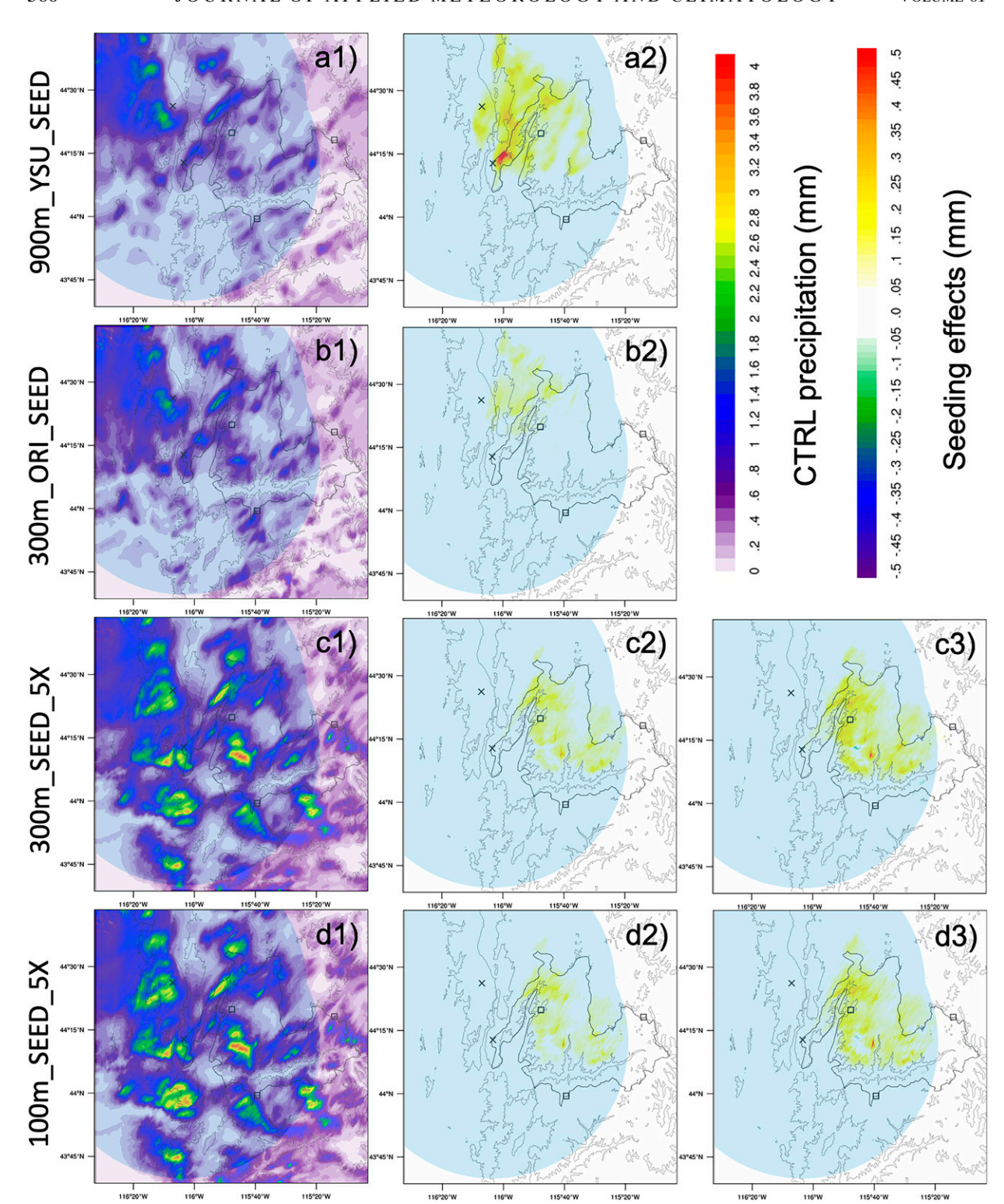


Fig. 15. Accumulated natural (CTRL) precipitation (mm) from 1640 to 1820 UTC for (a1) 900m_YSU_CTRL, (b1) 300m_ORI_CTRL, (c1) 300m_CTRL, and (d1) 100m_CTRL. Also shown are the corresponding seeding effects (precipitation difference between the SEED and CTRL simulations; mm) for (a2) 900m_YSU_SEED, (b2) 300m_ORI_SEED, (c2) 300m_SEED, (c3) 300m_SEED_5X, (d2) 100m_SEED, and (d3) 100m_SEED_5X. Only the values within the 100-m LES domain are shown. The blue semitransparent shaded area in each panel indicates the combined DOW detection range. The crosses and squares have the same meanings as those in Fig. 1b.

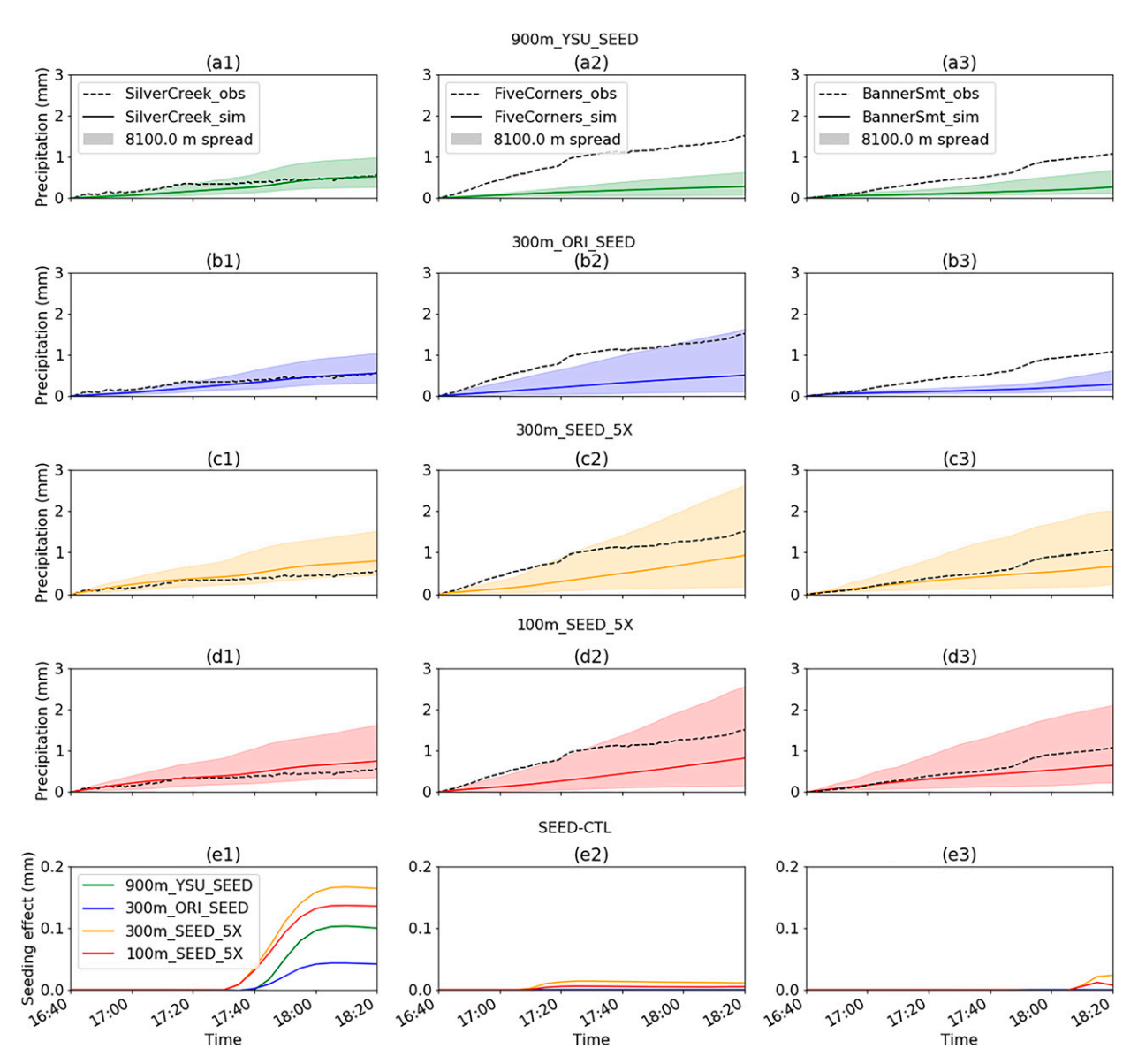


FIG. 16. Time series of observed (black dashed lines) and simulated precipitation (color lines and shaded areas) over (a1),(b1),(c1),(d1) Silver Creek; (a2),(b2),(c2),(d2) Five Corners; and (a3),(b3),(c3),(d3) Banner Summit. The shaded areas indicate the spreads of simulated precipitation over an $8.1 \times 8.1 \text{ km}^2$ square centered at the gauge site. Also shown are (e1)–(e3) the averaged seeding effects within the square. The results from 900m_YSU_SEED are in green, those from 300m_ORI_SEED are in blue, those from 300m_SEED_5X are in orange, and those from 100m_SEED_5X are in red.

simulations. Also listed are the seeding-impacted areas in km² defined as the areas of grid points with seeding effect greater than 0.01 mm. The values are calculated within the 100-m LES domain and within the DOW detection range (blue shaded areas in Fig. 15) for the period used in the observational study between 1640 and 1810 UTC (Friedrich et al. 2020). The range of DOW-estimated seeding effects and seeding-impacted areas during the same period are listed for reference too.

It is found that the natural precipitation is sensitive to CCN background (~11% difference between 900m_ERA5_CTRL and 900m_03CCN_CTRL), IN background (~18% between

900m_MEYERS_CTRL and 900m_03CCN_CTRL), PBL representation (~24% between 900m_YSU_CTRL and 900m_03CCN_CTRL), and grid spacing (~12% between 300m_ORI_CTRL and 900m_YSU_CTRL) in this case. It is most sensitive to the wind field that leads to a relative change of more than 88% between 300m_CTRL and 300m_ORI_CTRL. Under the updated wind conditions, increase of resolution produces less than 2% difference between 100m_CTRL and 300m_CTRL. The simulated seeding effects are more sensitive to the following factors: ~73% by CCN background, ~66% by INP background, ~28% by PBL representation, ~15%-67% by grid spacing, and ~47% by wind field, and ~52%-56% by AgI

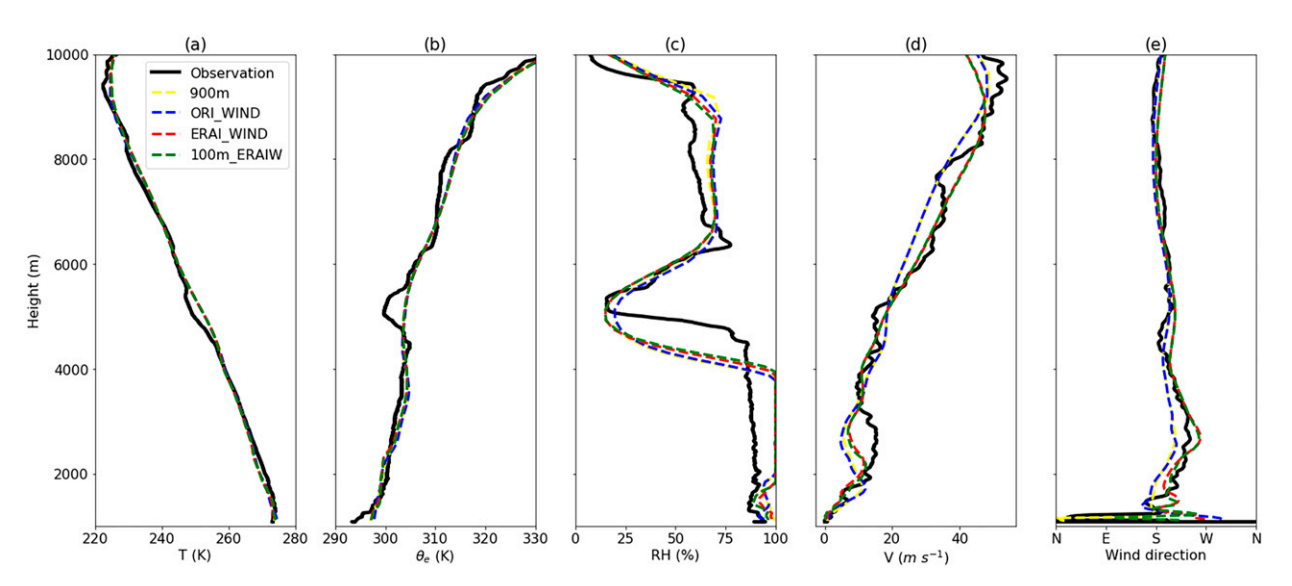


FIG. A1. As in Fig. 5, but for 900m_ERA5_CTRL (yellow dashed line marked as "900m"), 300m_ORI_CTRL (blue dashed line marked as "ORI_WIND"), 300m_CTRL (red dashed line marked as "ERAI_WIND"), and 100m_CTRL (green dashed line marked as "100m_ERAIW").

nucleation rate. The simulated seeding effects range from 65 to 331 af $(8.0-40.8 \times 10^4 \text{ m}^3)$ with a mean of 164 af $(20.2 \times 10^4 \text{ m}^3)$, which has a higher upper bound and higher mean than the observed range $(64-157 \text{ af or } 7.9-19.4 \times 10^4 \text{ m}^3)$ and mean $(100 \text{ af or } 12.3 \times 10^4 \text{ m}^3)$. The simulated seeding effects are inversely proportional to the natural precipitation or precipitation efficiency in most of the seeding simulations with 900-m grid spacing (Table 3). This finding is consistent with those found in Xue et al. (2013a,b) and Geresdi et al. (2017, 2020). The relative seeding effects range from 1.5% to 9.1% and the seeding-impacted areas vary between 1716 and 3135 km². The mean simulated seeding-impacted area is 2402 km^2 , which is very close to the observation-derived value of 2327 km² (Friedrich et al. 2020).

Based on the model–observation comparisons in previous sections, the LES runs with the updated wind field are more representative than other simulations. The mean seeding effect and seeding-impacted area of 300m_SEED, 300m_SEED_5X, $100m_SEED$, and $100m_SEED_5X$ simulations are 141 af $(17.4 \times 10^4 \text{ m}^3)$ and 2331 km², which are also in better agreement with the observed values relative to other seeding simulations.

5. Discussion

High-quality observations of environmental conditions, cloud structure, microphysical properties, and precipitation from various platforms and instruments have been collected in IOP5 of the SNOWIE field campaign, which allow us to evaluate the WRF-WxMod seeding simulations in great detail. During this IOP, a strong dry-air intrusion due to the tropopause folding split the deep precipitating cloud into two layers. The deep, very dry and clean air layer prevented the seeder–feeder process from happening and provided few INP

to nucleate ice and grow in the lower orographic clouds over the target area during the seeding period. Aircraft in situ data show that the lower-layer cloud top (temperature around -15° C) mostly consisted of supercooled cloud droplets and drizzle drops.

Four commonly used reanalysis datasets were tested using a single domain with 900-m grid spacing. The ERA5 simulations were found to be most representative, based on a comparison of simulated soundings and cloud structures with observations. The WRF model with the Thompson–Eidhammer microphysics scheme and the DeMott2010 INP parameterization faithfully reproduced the double-layer cloud structure and a supercooled liquid cloud top of the lower, orographic clouds. In the cloud-top region, the DeMott2010 INP parameterization produced negligible ice particles around -15° C (not shown).

The CCN concentration input to the model was scaled down to 30% of the climatological value and the YSU PBL was used in the WRF-WxMod 900-m simulation to better capture the observed supercooled liquid water properties (number concentration, LWC and LWP). The results of this "most representative" 900-m single domain simulation (900m_YSU_CTRL) were processed to generate initial and lateral boundary conditions for LES seeding simulations.

The comparisons of the seeding plume morphology and locations between DOW-derived data and model results indicate that the wind field needed to be adjusted to realistically simulate the seeding impacts on clouds and precipitation. The LES runs with the wind tendencies provided by 900m_ERAI_CTRL were found to be in better agreement with observed cloud and precipitation properties associated with seeding.

The WRF-WxMod seeding simulations showed that the number of AgI-nucleated ice particles in the cloud-top region increases with grid spacing, owing to increased AgI

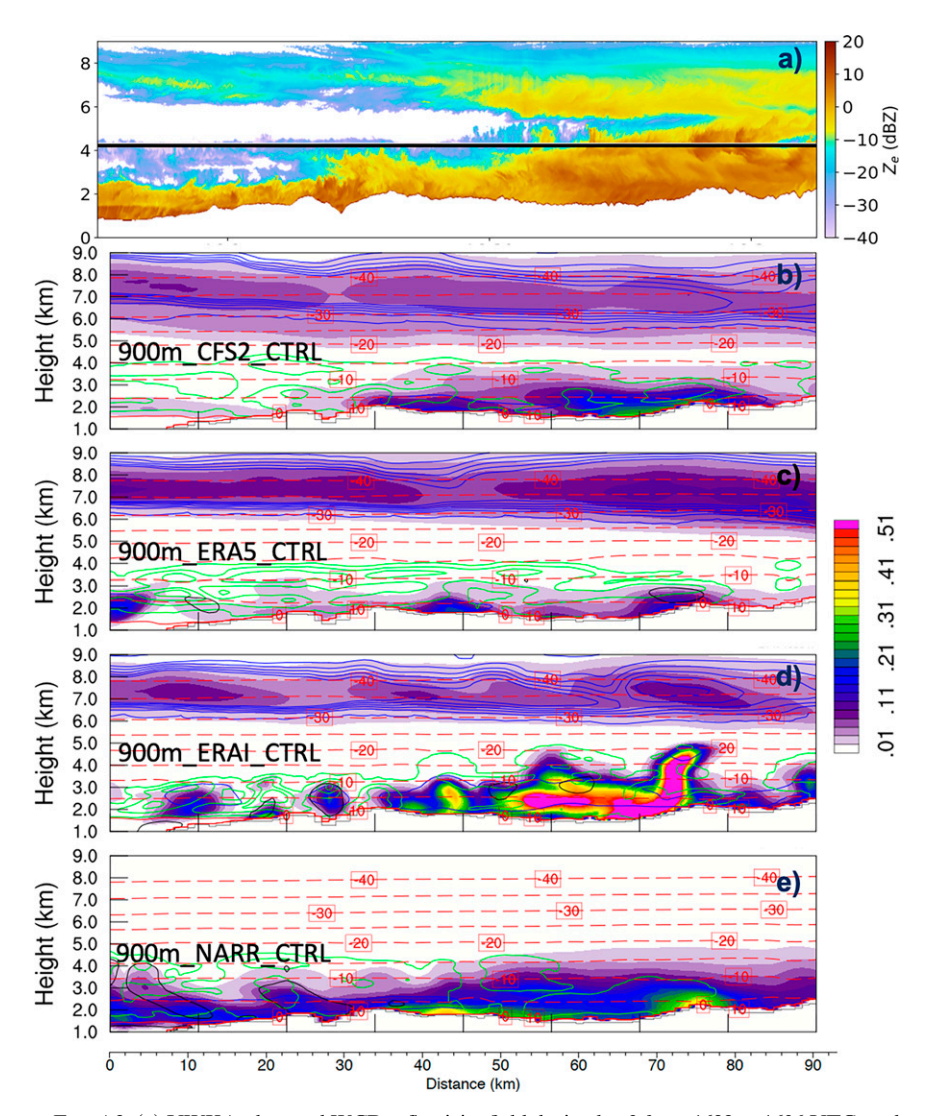


FIG. A2. (a) UWKA observed WCR reflectivity field during leg 3 from 1622 to 1636 UTC, and the corresponding model-based cross sections at 1625 UTC for (b) 900m_CFS2_CTRL, (c) 900m_ERA5_CTRL, (d) 900m_ERAI_CTRL, and (e) 900m_NARR_CTRL. Color shading is the snow mixing ratio (g kg $^{-1}$). Ice number concentrations (L $^{-1}$) are in blue contours starting at 1 L $^{-1}$ with an interval of 20 L $^{-1}$. Cloud and rain water mixing ratios (g kg $^{-1}$) are respectively in green and black contours starting at 0.01 g kg $^{-1}$ with an interval of 0.1 g kg $^{-1}$. Red dashed lines represent temperature (°C). Southwest is on the left, and northeast is on the right.

dispersion. The simulated PNC100 inside the seeding plumes are of the same magnitude as the observed values along the UWKA tracks. The values are higher when the AgI nucleation rate is increased. The simulated seeding effects on precipitation have a positive relationship with the PNC100 and the number of AgI-nucleated ice particles in the cloud-top region. The simulated natural precipitation and seeding effects are sensitive to the CCN, INP background, and PBL physics.

Uncertainties in observations and simulations as well as disagreements between them are inevitable regardless how carefully the numerical experiments are designed. Quantitative

evaluations of the performance of individual simulation in a large parameter space are challenging given the observation and model uncertainties. Nonetheless, the simulated seeding effects on precipitation from all seeding simulations agreed with the DOW-derived values in terms of the range, mean value and impacted areas, with slight overestimates. The seeding effects in the four LES runs are in better agreement with the observed values when the updated wind fields are used. This finding inspires us to design an approach of observation-constrained ensemble seeding simulations using multiple reanalysis data and physics and to develop quantitative evaluation methods to better quantify the seeding impacts with

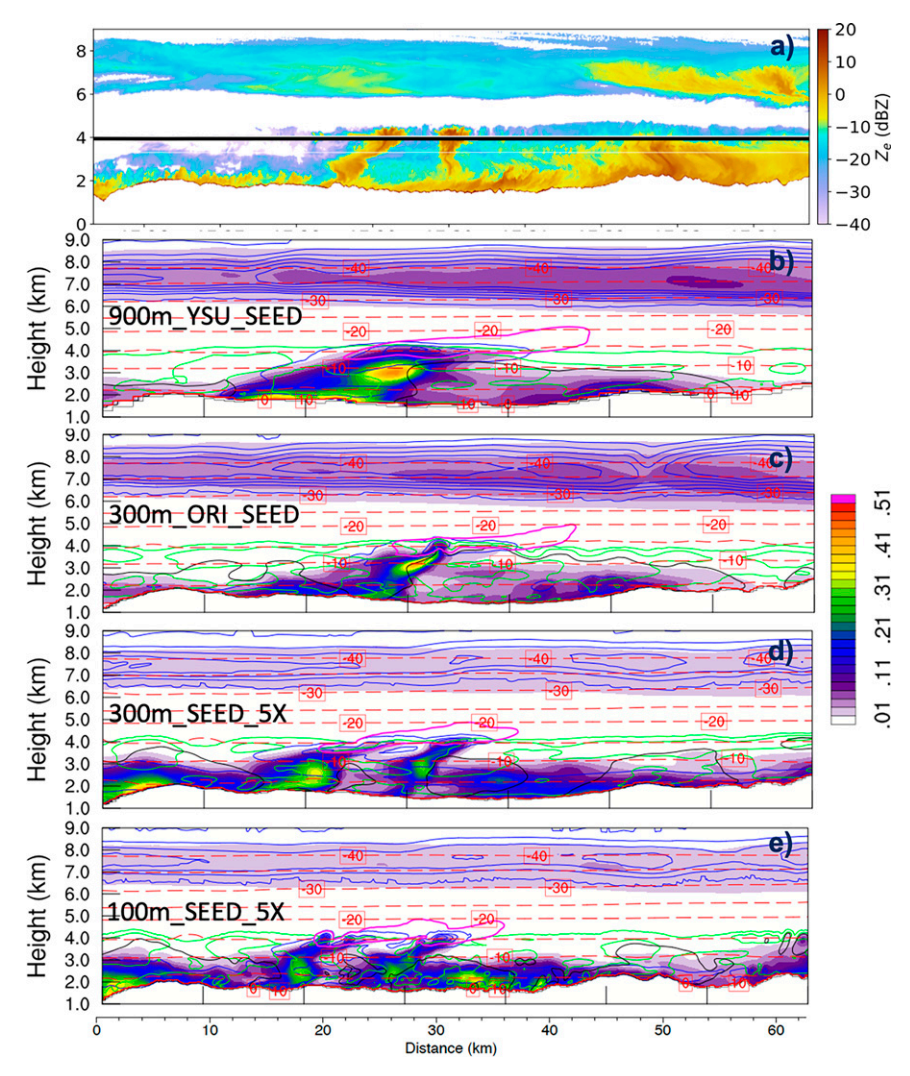


FIG. A3. Similar to Fig. A2, but for (a) UWKA WCR reflectivity during leg 7, showing (b) $900m_YSU_SEED$, (b) $300m_ORI_SEED$, (d) $300m_SEED_5X$, and (e) $100m_SEED_5X$ at 1730 UTC. In (b)–(e), the purple contours represent the dry AgI particle number concentration (10^5 m⁻³).

uncertainty estimation at the same time. The description of the approach and the results based on the IOP5 simulations will be covered and discussed in a separate paper.

6. Conclusions

French et al. (2018) and Friedrich et al. (2020 2021) describe the impact of airborne glaciogenic seeding of a shallow orographic cloud with a supercooled liquid cloud top at around -15°C, observed on 19 January 2017 as part of the SNOWIE campaign, designed around an operational seeding program in Idaho (Tessendorf et al. 2019). Here, we numerically simulate this event and the seeding impact using the WRF-WxMod model at high resolutions. Our key findings and conclusions are as follows:

- Reproducing the observed cloud structure and seeding plume dispersion pattern is difficult, given the paucity of meteorological data: we found a high sensitivity to the choice of the driver dataset. The ERA5 reanalysis dataset, with prerequisite corrections to the wind field, proved to be most representative.
- No detailed measurements of upstream cloud-active aerosol concentrations were available, but we found that the Thompson-Eidhammer microphysics scheme with a CCN concentration 30% of the climatology reproduces observed cloud structure and supercooled liquid water properties well.
- This experimentally optimized WRF-WxMod configuration is able to simulate the observed features and evolution of seeded clouds and precipitation reasonably well, especially when it is run in LES mode.

This bodes well for the use of well-validated numerical simulations for the quantification of cumulative precipitation enhancement by seasonal seeding programs, such as the one in Idaho. Significant uncertainties remain, given the diversity of cloud and precipitation systems.

Acknowledgments. This research was supported by Idaho Power Company and National Science Foundation (NSF) Grants AGS-1547101, AGS-1546963, AGS-1546939, AGS-2016106, AGS-2015829, and AGS-2016077. Funding for the UWKA and WCR during SNOWIE was provided through the NSF Award AGS-1441831. Funding for CSWR-DOWs was provided through NSF AGS-1441831. The authors thank Robert Capella for his assistance in producing Figs. 2 and 3. The helpful suggestions from Jimy Dudhia for addressing review comments are greatly appreciated. The National Center for Atmospheric Research is sponsored by NSF.

Data availability statement. The SNOWIE observational data are available through the NCAR EOL website (https://www.eol.ucar.edu/field_projects/snowie). The simulation data are available through the NCAR campaign data storage upon request.

APPENDIX

Additional Sounding and Cloud Structure Figures

Figures A1–A3 show extra sounding and cloud structure comparisons between model results and observations.

REFERENCES

- Atlas, R. L., C. S. Bretherton, P. N. Blossey, A. Gettelman, C. Bardeen, P. Lin, and Y. Ming, 2020: How well do largeeddy simulations and global climate models represent observed boundary layer structures and low clouds over the summertime Southern Ocean? J. Adv. Model. Earth Sys., 12, e2020MS002205, https://doi.org/10.1029/2020MS002205.
- Breed, D., R. Rasmussen, C. Weeks, B. Boe, and T. Deshler, 2014: Evaluating winter orographic cloud seeding: Design of the Wyoming Weather Modification Pilot Project (WWMPP). J. Appl. Meteor. Climatol., 53, 282–299, https://doi.org/10.1175/ JAMC-D-13-0128.1.
- Chen, Q., J. Fan, S. Hagos, W. I. Gustafson Jr., and L. K. Berg, 2015: Roles of wind shear at different vertical levels: Cloud system organization and properties. *J. Geophys. Res. Atmos.*, 120, 6551–6574, https://doi.org/10.1002/2015JD023253.
- Chu, X., L. Xue, B. Geerts, R. Rasmussen, and D. Breed, 2014: A case study of radar observations and WRF LES simulations of the impact of ground-based glaciogenic seeding on orographic clouds and precipitation. Part I: Observations and model validations. *J. Appl. Meteor. Climatol.*, 53, 2264–2286, https://doi.org/10.1175/JAMC-D-14-0017.1.
- ——, B. Geerts, L. Xue, and B. Pokharel, 2017a: A case study of cloud radar observations and large-eddy simulations of a shallow stratiform orographic cloud, and the impact of

- glaciogenic seeding. *J. Appl. Meteor. Climatol.*, **56**, 1285–1304, https://doi.org/10.1175/JAMC-D-16-0364.1.
- —, —, and R. Rasmussen, 2017b: Large-eddy simulations of the impact of ground-based glaciogenic seeding on shallow orographic convection: A case study. *J. Appl. Meteor. Climatol.*, **56**, 69–84, https://doi.org/10.1175/JAMC-D-16-0191.1.
- Dee, D. P., and Coauthors, 2011: The ERA-interim reanalysis: Configuration and performance of the data assimilation system. *Quart. J. Roy. Meteor. Soc.*, **137**, 553–597, https://doi.org/10.1002/gi.828.
- DeMott, P. J., and Coauthors, 2010: Predicting global atmospheric ice nuclei distributions and their impacts on climate. *Proc. Natl. Acad. Sci. USA*, **107**, 11217–11222, https://doi.org/10. 1073/pnas.0910818107.
- Flossmann, A. I., M. Manton, A. Abshaev, R. Bruintjes, M. Murakami, T. Prabhakaran, and Z. Yao, 2019: Review of advances in precipitation enhancement research. *Bull. Amer. Meteor. Soc.*, **100**, 1465–1480, https://doi.org/10.1175/ BAMS-D-18-0160.1.
- Friedrich, K., and Coauthors, 2020: Quantifying snowfall from orographic cloud seeding. *Proc. Natl. Acad. Sci. USA*, 117, 5190–5195, https://doi.org/10.1073/pnas.1917204117.
- —, and Coauthors, 2021: Microphysical characteristics and evolution of seeded orographic clouds. *J. Appl. Meteor. Climatol.*, 60, 909–934, https://doi.org/10.1175/JAMC-D-20-0206.1.
- French, J. R., and Coauthors, 2018: Precipitation formation from orographic cloud seeding. *Proc. Natl. Acad. Sci. USA*, 115, 1168–1173, https://doi.org/10.1073/pnas.1716995115.
- Geerts, B., and Coauthors, 2013: The AgI Seeding Cloud Impact Investigation (ASCII) campaign 2012: Overview and preliminary results. J. Wea. Modif., 45, 24–43.
- Geresdi, I., L. Xue, and R. Rasmussen, 2017: Evaluation of orographic cloud seeding using bin microphysics scheme: Two-dimensional approach. *J. Appl. Meteor. Climatol.*, 56, 1443–1462, https://doi.org/10.1175/JAMC-D-16-0045.1.
- —, —, N. Sarkadi, and R. Rasmussen, 2020: Evaluation of orographic cloud seeding using bin microphysics scheme: Three-dimensional simulation of real cases. *J. Appl. Meteor. Climatol.*, **59**, 1537–1555, https://doi.org/10.1175/JAMC-D-19-0278 1
- Hersbach, H., and Coauthors, 2020: The ERA5 global reanalysis. *Quart. J. Roy. Meteor. Soc.*, **146**, 1999–2049, https://doi.org/10.1002/qj.3803.
- Hodge, M. W., 1956: Superadiabatic lapse rates of temperature in radiosonde observations. *Mon. Wea. Rev.*, **84**, 103–106, https://doi.org/10.1175/1520-0493(1956)084<0103:SLROTI>2. 0.CO:2.
- Hong, S.-Y., Y. Noh, and J. Dudhia, 2006: A new vertical diffusion package with an explicit treatment of entrainment processes. *Mon. Wea. Rev.*, 134, 2318–2341, https://doi.org/10.1175/MWR3199.1.
- Jing, X., and B. Geerts, 2015: Dual-polarization radar data analysis of the impact of ground-based glaciogenic seeding on winter orographic clouds. Part II: Convective clouds. *J. Appl. Meteor. Climatol.*, **54**, 2099–2117, https://doi.org/10.1175/JAMC-D-15-0056.1.
- —, —, K. Friedrich, and B. Pokharel, 2015: Dual-polarization radar data analysis of the impact of ground-based glaciogenic seeding on winter orographic clouds. Part I: Mostly stratiform clouds. *J. Appl. Meteor. Climatol.*, **54**, 1944–1969, https://doi. org/10.1175/JAMC-D-14-0257.1.
- —, —, Y. Wang, and C. Liu, 2017: Evaluating seasonal orographic precipitation in the interior western United States

- using gauge data, gridded precipitation estimates, and a regional climate simulation. *J. Hydrometeor.*, **18**, 2541–2558, https://doi.org/10.1175/JHM-D-17-0056.1.
- Kala, J., J. Andrys, T. J. Lyons, I. J. Foster, and B. J. Evans, 2015: Sensitivity of WRF to driving data and physics options on a seasonal time-scale for the southwest of Western Australia. Climate Dyn., 44, 633–659, https://doi.org/10.1007/s00382-014-2160-2.
- Keeler, J. M., R. M. Rauber, B. F. Jewett, G. M. McFarquhar, R. M. Rasmussen, L. Xue, C. Liu, and G. Thompson, 2017: Dynamics of cloud-top generating cells in winter cyclones. Part III: Shear and convective organization. *J. Atmos. Sci.*, 74, 2879–2897, https://doi.org/10.1175/JAS-D-16-0314.1.
- Mahrer, Y., 1984: An improved numerical approximation of the horizontal gradients in a terrain-following coordinate system. *Mon. Wea. Rev.*, 112, 918–922, https://doi.org/10.1175/1520-0493(1984)112<0918:AINAOT>2.0.CO;2.
- Majewski, A., and J. French, 2020: Supercooled drizzle development in response to semi-coherent vertical velocity fluctuations within an orographic-layer cloud. *Atmos. Chem. Phys.*, 20, 5035–5054, https://doi.org/10.5194/acp-20-5035-2020.
- Mesinger, F., and Coauthors, 2006: North American Regional Reanalysis. Bull. Amer. Meteor. Soc., 87, 343–360, https://doi. org/10.1175/BAMS-87-3-343.
- Meyers, M. P., P. J. DeMott, and W. R. Cotton, 1992: New primary ice-nucleation parameterizations in an explicit cloud model. *J. Appl. Meteor.*, 31, 708–721, https://doi.org/10.1175/1520-0450(1992)031<0708:NPINPI>2.0.CO;2.
- Morrison, H., and Coauthors, 2020: Confronting the challenge of modeling cloud and precipitation microphysics. J. Adv. Model. Earth Syst., 12, e2019MS001689, https://doi.org/10. 1029/2019MS001689.
- Nakanishi, M., and H. Niino, 2004: An improved Mellor–Yamada level-3 model with condensation physics: Its design and verification. *Bound.-Layer Meteor.*, **112**, 1–31, https://doi.org/10.1023/B:BOUN.000020164.04146.98.
- —, and —, 2006: An improved Mellor–Yamada level-3 model: Its numerical stability and application to a regional prediction of advection fog. *Bound.-Layer Meteor.*, **119**, 397–407, https://doi.org/10.1007/s10546-005-9030-8.
- Niu, G., Z. L. Yang, K. Mitchell, F. Chen, M. Ek, M. Barlage, and Y. Xia, 2011: The community Noah land surface model with multiparametrization options (Noah-MP): 1. Model description and evaluation with local-scale measurements. *J. Geo*phys. Res., 116, D12109, https://doi.org/10.1029/2010JD015139.
- Oue, M., A. Tatarevic, P. Kollias, D. Wang, K. Yu, and A. M. Vogelmann, 2020: The Cloud-Resolving Model Radar Simulator (CR-SIM) Version 3.3: Description and applications of a virtual observatory. *Geosci. Model Dev.*, 13, 1975–1998, https://doi.org/10.5194/gmd-13-1975-2020.
- Pincus, R., H. W. Barker, and J.-J. Morcrette, 2003: A fast, flexible, approximate technique for computing radiative transfer in inhomogeneous cloud fields. J. Geophys. Res., 108, 4376, https://doi.org/10.1029/2002JD003322.
- Pokharel, B., and B. Geerts, 2016: A multi-sensor study of the impact of ground-based glaciogenic seeding on clouds and precipitation over mountains in Wyoming. Part I: Project description. Atmos. Res., 182, 269–281, https://doi.org/10.1016/ j.atmosres.2016.08.008.
- —, and X. Jing, 2014a: The impact of ground-based glaciogenic seeding on orographic clouds and precipitation: A multi-sensor case study. *J. Appl. Meteor. Climatol.*, **53**, 890–909, https://doi.org/10.1175/JAMC-D-13-0290.1.

- —, —, K. Friedrich, J. Aikins, D. Breed, R. Rasmussen, and A. Huggins, 2014b: The impact of ground-based glaciogenic seeding on clouds and precipitation over mountains: A multi-sensor case study of shallow precipitating orographic cumuli. *Atmos. Res.*, 147–148, 162–182, https://doi.org/10.1016/j.atmosres.2014.05.014.
- —, —, and —, 2015: The impact of ground-based glaciogenic seeding on clouds and precipitation over mountains: A case study of a shallow orographic cloud with large supercooled droplets. *J. Geophys. Res. Atmos.*, **120**, 6056–6079, https://doi.org/10.1002/2014JD022693.
- —, —, K. Friedrich, K. Ikeda, and R. Rasmussen, 2017:
 A multi-sensor study of the impact of ground-based glaciogenic seeding on clouds and precipitation over mountains in Wyoming. Part II: Seeding impact analysis. *Atmos. Res.*, **183**, 42–57, https://doi.org/10.1016/j.atmosres.2016.08.018.
- Rasmussen, R. M., and Coauthors, 2018: Evaluation of the Wyoming Weather Modification Pilot Project (WWMPP) using two approaches: Traditional statistics and ensemble modeling. *J. Appl. Meteor. Climatol.*, 57, 2639–2660, https://doi.org/10.1175/JAMC-D-17-0335.1.
- Rauber, R. M., and Coauthors, 2019: Wintertime orographic cloud seeding—A review. J. Appl. Meteor. Climatol., 58, 2117–2140, https://doi.org/10.1175/JAMC-D-18-0341.1.
- Saha, S., and Coauthors, 2014: The NCEP Climate Forecast System version 2. *J. Climate*, **27**, 2185–2208, https://doi.org/10.1175/JCLI-D-12-00823.1.
- Slonaker, R. L., B. E. Schwartz, and W. J. Emery, 1996: Occurrence of nonsurface superadiabatic lapse rates within RAOB data. Wea. Forecasting, 11, 350–359, https://doi.org/10.1175/1520-0434(1996)011<0350:OONSLR>2.0.CO;2.
- Tessendorf, S. A., and Coauthors, 2019: Transformational approach to winter orographic weather modification research: The SNOWIE Project. *Bull. Amer. Meteor. Soc.*, **100**, 71–92, https://doi.org/10.1175/BAMS-D-17-0152.1.
- Thompson, G., and T. Eidhammer, 2014: A study of aerosol impacts on clouds and precipitation development in a large winter cyclone. J. Atmos. Sci., 71, 3636–3658, https://doi.org/ 10.1175/JAS-D-13-0305.1.
- —, P. R. Field, W. R. Hall, and R. Rasmussen, 2008: Explicit forecasts of winter precipitation using an improved bulk microphysics scheme. Part II: Implementation of a new snow parameterization. *Mon. Wea. Rev.*, 136, 5095–5115, https://doi.org/10.1175/2008MWR2387.1.
- Xue, L., A. Teller, R. Rasmussen, I. Geresdi, and Z. Pan, 2010: Effects of aerosol solubility and regeneration on warm-phase orographic clouds and precipitation simulated by a detailed bin microphysical scheme. J. Atmos. Sci., 67, 3336–3354, https://doi.org/10.1175/2010JAS3511.1.
- —, and Coauthors, 2013a: Implementation of a silver iodide cloud seeding parameterization in WRF. Part I: Model description and idealized 2D sensitivity tests. *J. Appl. Meteor. Climatol.*, **52**, 1433–1457, https://doi.org/10.1175/JAMC-D-12-0148.1.
- —, S. A. Tessendorf, E. Nelson, R. Rasmussen, D. Breed, S. Parkinson, P. Holbrook, and D. Blestrud, 2013b: Implementation of a silver iodide cloud seeding parameterization in WRF. Part II: 3D simulations of actual seeding events and sensitivity tests. *J. Appl. Meteor. Climatol.*, 52, 1458–1476, https://doi.org/10.1175/JAMC-D-12-0149.1.
- —, X. Chu, R. Rasmussen, D. Breed, B. Boe, and B. Geerts, 2014: The dispersion of silver iodide particles from groundbased generators over complex terrain. Part 2: WRF large-

- eddy simulations versus observations. *J. Appl. Meteor. Climatol.*, **53**, 1342–1361, https://doi.org/10.1175/JAMC-D-13-0241.1.

 —, —, —, and B. Geerts, 2016: A case study of radar observations and WRF LES simulations of the impact of ground-based glaciogenic seeding on orographic clouds and precipitation. Part II: AgI dispersion and seeding signals
- simulated by WRF. J. Appl. Meteor. Climatol., **55**, 445–464, https://doi.org/10.1175/JAMC-D-15-0115.1.
- —, and Coauthors, 2017: WRF large-eddy simulations of chemical tracer deposition and seeding effect over complex terrain from ground- and aircraft-based AgI generators. *Atmos. Res.*, 190, 89–103, https://doi.org/10.1016/j.atmosres.2017.02.013.